TWDB Contract No. 2101792506
Final Report
Received: April 13, 2022

BUREAU OF ECONOMIC GEOLOGY
THE UNIVERSITY OF TEXAS AT AUSTIN
University Station, Box X • Austin, Texas 78713-8924 • (512) 471-1534 • FAX (512) 471-0140
10100 Burnet Road, Bldg. 130 • Austin, Texas 78758-4497

Airborne Lidar bathymetry and multi-band satellite imaging analysis of Lower Laguna Madre, TX

Final Report

Texas Water Development Board

Contract# 2101792506

Principal Investigator: Kutalmis Saylam

Satellite Imaging Analysis: Alejandra Briseno

Near Surface Observatory,
Bureau of Economic Geology,
John A. and Katherine G. Jackson School of Geosciences,
The University of Texas at Austin

Table of Contents

Abstract 3

1) Introduction 3

2) Materials and Methods 6

a) Project location 7

b) Mapping with airborne Lidar systems 7

(a) Airborne Lidar bathymetry 9

c) Quality assurance and quality control (QA and QC) 12

i) ALB system calibration 14

ii) *In-situ* measurements 17

iii) Vector data analysis 22

d) Lidar data acquisition 24

e) Satellite imaging analysis 25

i) Imagery downloads and preparation 25

ii) Reflectance 27

iii) Bathymetry 28

3) On site analysis 29

4) Results 31

a) Reflectance 31

f) Lidar bathymetry 35

g) Satellite derived bathymetry (SDB) 44

h) SDB-based spatio-temporal analysis 50

i) Lidar topography 53

5) Conclusions 56

Acknowledgement 57

References 58

Appendix A - Data acquisition mission log 62

Appendix B - Turbidity and localized sonar measurements 65

Appendix C - Reflectance 68

Appendix D – Satellite derived bathymetry 73

Abstract

In 2017, Bureau of Economic Geology researchers at the University of Texas at Austin, acquired topographic and bathymetric airborne Lidar data over Lower Laguna Madre, which is a shallow hypersaline estuary at the southern end of Texas. The nature of this data acquisition campaign was unique due to size (1600 km^2) and the dynamic environmental conditions that influenced the depth and water quality. Researchers acquired 60 hours of airborne Lidar data and completed *in-situ* measurements from a boat to quantify water quality and depths. Data analysis included processing Sentinel-2 L1C satellite imagery to predict water quality and to determine areas with high turbidity. To confirm the topographic heights and water depths, Lidar measurements were compared to GPS elevations, sonar, and satellite bathymetry using least-squares algorithm. Because ALB technology is superior in detail compared to satellite bathymetry, results produced skewed distribution for satellite bathymetry with an average depth disparity of 6-25 cm (RMSE of 22-35 cm) where water depths were shallower than 1.5 m. The study concluded that satellite bathymetry can be a cost-effective method to complement ALB mapping efforts; however, varying environmental conditions, bottom properties and tidal influences have a direct impact on depth accuracy and wholeness of data sets.

1) Introduction

Remote sensing is an advanced imaging technology that enables information retrieval of objects and measuring targeted surfaces from a distance using an active or passive propagated electromagnetic energy (EM, **Figure 1**). Passive remote sensing techniques measure the ambient EM energy reflected by target surfaces, allowing researchers to detect and characterize features through recorded variable spectral responses (Khorram, 2012; Thenkabail, 2018). In the recent years, use of active remote sensing technologies from an airborne platform (orbiting satellite or an aircraft) has become increasingly popular to measure the topography of hard surfaces or the depths of relatively shallow and transparent waters. Therefore, a number of projects investigated and used the technology towards coastal applications such as shoreline mapping, erosion and change detection (Brock and Purkis, 2009; Klemas,

2011; Paine et al., 2017). Added to the depth measurement capabilities, topographic data acquisition capacity of airborne platforms has led to initiating new and diverse research projects.

The Bureau of Economic Geology (BEG, The Bureau) at the University of Texas at Austin has been involved in airborne Lidar surveys (ALS) for nearly two decades. The Bureau has initiated and completed numerous airborne topographic airborne Light Detection and Ranging (Lidar) surveys using an Optech Airborne Laser Terrain Mapper (ALTM) ALS, applying specific best practices and quality management procedures to a diverse range of applications since 2002 (Saylam et al., 2018b).

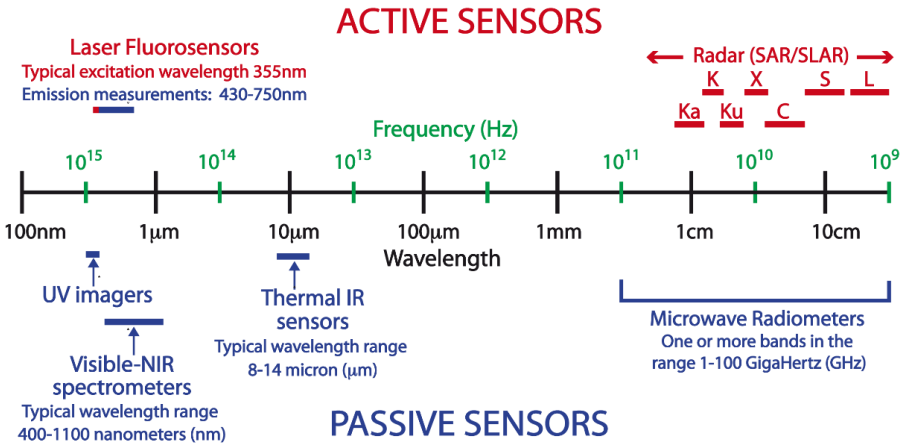

Figure 1: Electromagnetic energy spectrum and wavelength dispersion of active and passive sensors (Muller, 2017).

In 2012, BEG purchased a custom airborne Lidar system, manufactured by Airborne Hydrography AB (AHAB) of Sweden, with bathymetric measurement capability, named “Chiroptera”. Chiroptera uses a near-infrared (NIR, 1064 nm) wavelength for topographic data collection and a green-wavelength (visible, 515 nm) for bathymetric data collection. Over the years, BEG has established itself as a premier airborne Lidar research institution and contributed to the growing popularity of ALS science by initiating and completing several projects with diverse scopes. Some of these projects involved in determining the size and depth of thermo-karst lakes on the Alaskan North Slope (Paine et al., 2015; Saylam et al., 2017a), mapping of the shallow seafloor along the Gulf of Mexico and in the Pacific coast (Paine et al., 2017) and mapping bottom morphologies along various river sheds (Saylam et al., 2020, 2018a). Furthermore, BEG involved in a variety of applications to monitor the coastal (gulf and bay) environments to understand the susceptibility of coastal lands to tropical storm flooding and over-wash, and quantifying the hurricane impact and subsequent coastal recovery (Caudle et al., 2019; Paine et al., 2013).

In 2017, BEG researchers acquired topographic and bathymetric airborne Lidar data of Lower Laguna Madre, a hypersaline estuary in southern Texas (**Figure 2**). Airborne data acquisition covered bank-to-bank channel bathymetry of the entire lower lagoon, the South Padre Island shoreline, and the southerly-located inland water reservoirs as outlined with the yellow polygon in Figure 2. In addition to the airborne data acquisition, BEG researchers conducted localized *in-situ* measurements to quantify the water transparency and acquired sonar depths from a kayak to verify the accuracy of bathymetric measurements. The nature of this study was significantly different because of the area size (~ 1600 km^2) and the dynamic nature of the lagoon.

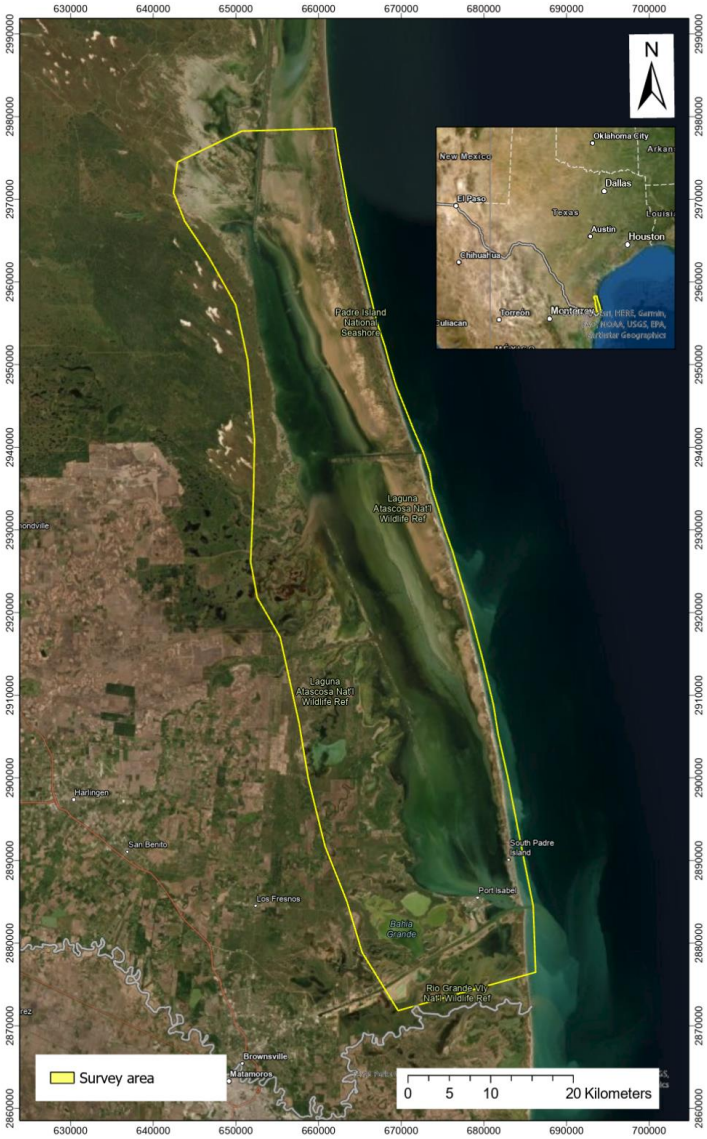

Figure 2: Lower Laguna Madre, the yellow polygon indicates the extent of the airborne Lidar survey area.

The survey area was fragmented into six sections (A-F) because of its size and the diverse ecologic nature of the lagoon (**Appendix A, Figure A-1**). Sections A, C and E included areas of hard surfaces and lagoon shoreline, where sections B and D contained primarily the lagoon waters. Section F, island causeway to the international border (U.S.A. to Mexico), is a mix of hard surfaces and include various inland reservoirs that are not a high priority in this project. BEG researchers completed preliminary data processing and analysis in Laguna Madre, immediately after each airborne mission. Investigation of water quality indicated high turbidity levels (> 5 Nephelometric unit, NTU) particularly in the south-west and central-east areas of the lagoon (Sections C, D and F), which was a challenge to measure depths using ALB technology.

In 2020, Texas Water Development Board (TWDB) contacted BEG and inquired about processing and analysis of Lower Laguna Madre airborne Lidar data sets, supplemented with multi-band satellite imagery. Statement of Work (SOW) proposed to address the following research aspects:

- Document data analysis methods by utilizing the archived satellite imagery and water quality data from Texas Commission on Environmental Quality (TCEQ),
- Support TWDB efforts by analyzing airborne Lidar bathymetry and identify the areas that requires multi-beam sonar surveys to build a complete chart mapping of the lagoon,
- Provide visual and statistical guidance to the understanding of the annual bathymetric changes in the lagoon by conducting a temporal analysis with satellite derived bathymetry,
- Compare and quantify the depth accuracy of airborne Lidar and satellite derived bathymetry,
- Document and publish results that reflect all relevant contractual efforts.

2) Materials and Methods

In dynamic coastal and fluvial environments, it is challenging to measure the water bottom in whole and with high accuracy using remote sensing methods. In this study, BEG proposed to supplement airborne Lidar with satellite derived bathymetry to support the understanding that these technologies are complementary, and combination of data can be an effective to map shallow waters (Ashphaq et al., 2021; Monteys et al., 2015; Najar et al., 2022). Literature supports that specific wavelengths such as the red-edge (690-730 nm) and the NIR (760-850 nm) have the potential to reveal chlorophyll-a, cyanobacteria, suspended and dissolved organic material concentrations in the water column (Bramich

et al., 2021; Johansen et al., 2018). Therefore, to understand the influence of water quality on airborne Lidar and satellite derived bathymetry, we proposed to study the recorded reflectance and classify the surfaces using multi-band satellite imagery.

a) Project location

In southern Texas, Lower Laguna Madre is a hypersaline (saltier than seawater) estuary that is physio-graphically divided into two subunits (McManus, 1990). Upper Laguna Madre is separated from the lower section of Laguna Madre by a land bridge, which is dredged as part of the Gulf Intracoastal Waterway (Tunnell and Judd, 2002). Lower Laguna Madre borders Mexico and the lagoon area covers an area larger than 800 km^2 (310 mi^2). The lagoon waters are relatively transparent and shallow in the middle and in the northern sections, but water quality is impacted by northerly winds that carry sedimentation from shoreline sand dunes and discharging freshwater streams. The lagoon has a unique seagrass ecosystem, protected by the Atascosa National Wildlife Refuge area in the north, and by Padre Island on the Gulf Coast. Seagrass beds serve as essential nursery areas for various Gulf of Mexico species and provide food and shelter for Redhead Ducks (*Aytha americana*). Because of the essential role that seagrass provides in support of fish and wildlife resources, a few studies have attempted to map the lagoon using other remote sensing technologies (Dubin et al., 2018; Webster et al., 2016).

b) Mapping with airborne Lidar systems

An airborne Lidar system (ALS) measures distances (ranges) for surface mapping purposes and includes several instruments on-board. A typical ALS integrates a laser power unit, a scanner mirror, transmitting and receiving units, Global Positioning System/Inertial Navigation System (GPS/INS), a digitizer, on-board storage, and an operator interface. The laser patterns (swath lines) on the target surfaces are generated by the rotation of the scanning mirror; they can be in (a) sawtooth (Z-shaped, oscillating), (b) parallel (rotating) or in (c) elliptical (nutating, Palmer) shapes (**Figures 3 a-c**). On board electronics measure the time-of-flight (TOF) duration of a Lidar beam travelling from the transmitter to the target surface and back to the receiver (echo). In a pulsed method (Equation 1), R is the slant distance, C is the speed of EM in the light form (~3×10^8 m/sec) and t_s equals to the TOF duration. In the continuous beam method (Equation 2), the range value is derived by comparing the transmitted and

received versions of the sinusoidal wave pattern of the emitted beam and measuring the phase difference between them (**Figure 4**). In Equation 2, *M* is the integer number of wavelengths, and λ is the known value of the wavelength. Delta (λ) is the fractional part of a wavelength defined by $\left(\frac{\varphi}{2\pi}\right) \times \lambda$, where φ is the phase angle.

$$R = (C \times t_s)/2 \qquad \text{(Equation 1)}$$

$$R = (\mathrm{M}\lambda + \Delta\lambda)/2 \qquad \text{(Equation 2)}$$

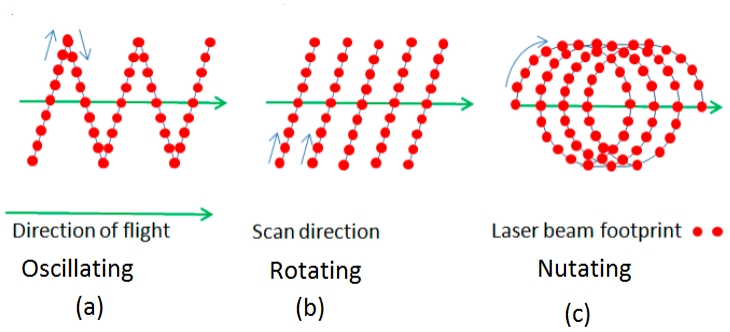

Figures 3 (a-c): Typical ALS scanning patterns: (A) oscillating mirror, (B) rotating and (C) Palmer (nutating) scan. Chiroptera emits light beams using a Palmer scanner that has the advantage of measuring the sloped water bottoms and the terrain underneath moderate canopied areas (modified after Fernandez-Diaz et al., 2014).

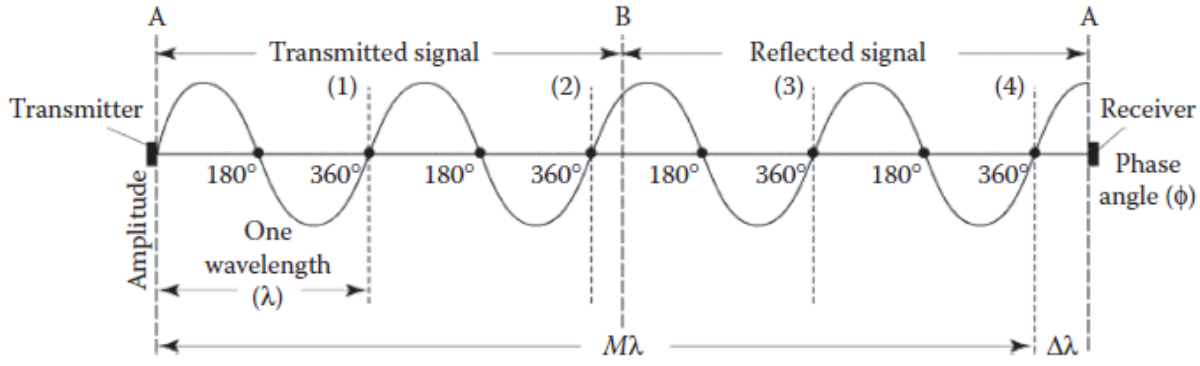

Figure 4: Phase comparison is calculated by comparing the transmitted and reflected signals from a continuous laser beam (Petrie and Toth, 2018).

(a) Airborne Lidar bathymetry

Airborne Lidar bathymetry (ALB) is an active, pulse-based, remote-sensing technology for mapping inland reservoirs and shorelines with relatively shallow and transparent waters. A typical ALB uses two laser transmitters: a near infrared wavelength (NIR, 1064 nm) to detect the water surface, and a green wavelength to detect the bottom and measure the depths (**Figure 5**). Green wavelength pulses (495-570 nm) have the least attenuation traversing through water until reaching and illuminating the bottom (Jerlov, 1976). In the water column, the light beam slows, and the amplitude attenuates rapidly due to natural refraction and scattering. If a beam does not attenuate, it reflects from the bottom and reaches back to the receiver (backscatter). The digitizer records the entire travel in a sinusoidal "waveform", indicating the surface, bottom, and all other major interactions with distinctive amplitude changes (**Figure 6**).

In Laguna Madre, BEG operated the Chiroptera at approximately 450 m above the water surface with a fixed pulse repetition rate of 35 kHz to acquire bathymetry. The NIR scanner acquired topographic data at varying rates of 100-300 kHz, – lower repetition rate at the higher altitudes.

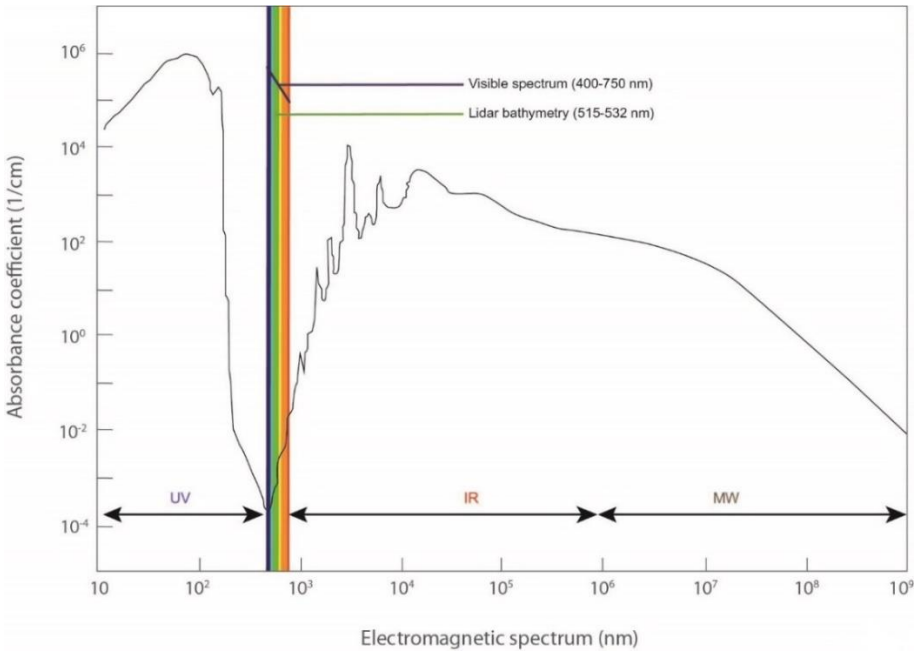

Figure 5: Representation of electromagnetic spectrum and showing the functional Lidar bathymetry optical range using the green wavelength in liquid water. Light pulses are minimally absorbed in the blue-green (450-570 nm) spectral region (modified after Beć and Huck, 2019).

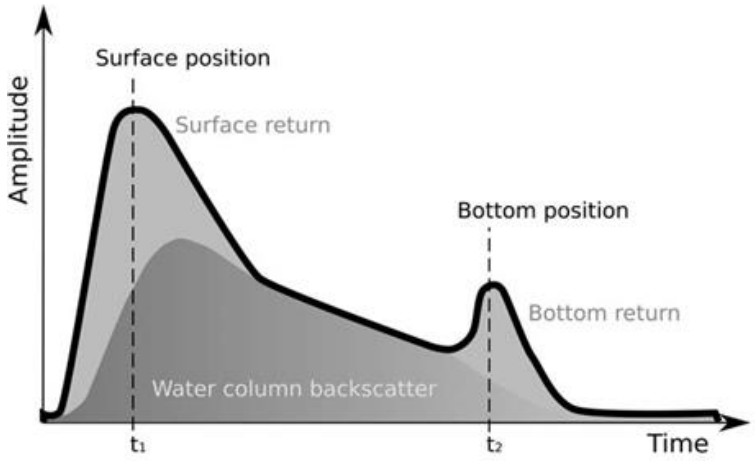

Figure 6: Conceptual representation of a green wavelength Lidar pulse, recorded as a waveform. Total time (Δt) represents the sampling difference between the peaks ($\Delta t = t_2 - t_1$) and defines the time marks when a light pulse hits the water surface (t_1), travels in the water column, reflects off the bottom (t_2) and leaves the water column (backscatter).

Using the ALB technology, water depths are calculated by computing the time difference (Δt) between the backscattering peaks of surface and bottom. The digitizer calculates the resulting time differences and considers variabilities recorded in the backscatter such as the electronic timing delays, interactions in the water-column, and the speed of light travelling in air and in water (2.25×10^8 m/s). In Equation (3), d_m is the distance travelled in meters and n is the refractive index of the water (n=1.33 to 1.34 at 20° degrees Celsius), Cw is the speed of light in the water, and f is the decoding speed in gigahertz (GHz). The value of refraction varies with the water temperature (T), the salinity (S, ‰) and the wavelength of the emitted beam (λ). To estimate the variability, we used Lidar data processing application tool (Lidar Survey Suite, LSS v2.40) that computes the surface representation using the refraction equation (Equation 4, Quan and Fry, 1995). It is also possible to compute the duration of each sample (t_d), by dividing the time difference (Δt) to system digitizer decoding speed (f) (Equation 5). Additionally, we can calculate the vertical spacing between the Lidar pulses, traveling in the space and in the water column. If we assume the refraction constant in the vacuum (n=1), each pulse spacing equals to 0.167 m. In the water, with the addition of refraction constant and the slowing light speed, the pulse spacing decreases. If we accept refraction constant as n=1.33, the spacing equals to 0.093 m between the pulses. **Table 1** presents the technical specifications of Chiroptera, indicating the fundamental differences between the NIR and green wavelength scanners. **Table 2** illustrates the conceptual

computation of pulse spacing and the consecutive depth measurement with each time sampling in the water.

$$d_m = \frac{C_w \Delta t}{2nf} \quad \text{Equation (3)}$$

$$n(S,T,\lambda) = n_0 + (n_1 + n_2 T + n_3 T^2)S + n_4 T^2 + \frac{n_5 + n_6 S + n_7 T}{\lambda} + \frac{n_8}{\lambda^2} + \frac{n_9}{\lambda^3} \quad \text{Equation (4)}$$

$$t_d = \frac{1}{f} \times \Delta t \quad \text{Equation (5)}$$

Table 1: Specifications of each Chiroptera ALB scanner. The beam divergence, pulse energy and peak power are substantially different among the NIR and green wavelength scanners.

Wavelength (nm)	**EM**	**Peak power (kW)**	**Pulse energy (μJ)**	**Pulse length (ns)**	**Beam divergence (mRad)**	**Pulse Repetition Rate (kHz)**
NIR (1064)	pulse	1.5 @250 kHz	30 @50 kHz 6 @250 kHz	4	0.5	10-400
Green (515)	waveform	38	> 100	2.5	3	36

Table 2: Computational parameters of measuring depths using the Chiroptera ALB system. In theory, depth equals to the two-way traverse time of the light pulse in the water, maintaining the same incident angle.

f **(GHz)**	**Interval (*i*)**	**Time tags (*Δt*)**	**Duration (sec)**	**Light in water (C_w,m/sec)**	***n***	**Traverse (W_{tr}) in water column (m)**	**Depth ($W_{tr}/2$) (m)**
1.8×10^9	5.56×10^{-10}	1	5.56×10^{-10}	2.25×10^8	1.33	0.094	0.047
		2	1.11×10^{-9}			0.187	0.094
		3	1.67×10^{-9}			0.281	0.141
		4	2.22×10^{-9}			0.375	0.188
		5	2.78×10^{-9}			0.469	0.235
		10	5.56×10^{-9}			0.939	0.47
		20	1.11×10^{-8}			1.879	0.94
		30	1.67×10^{-8}			2.819	1.41

c) Quality assurance and quality control (QA and QC)

In the literature, various articles discuss topographic Lidar quality control (QC) procedures and measures (e.g., Aguilar and Mills, 2008; Csanyi and Toth, 2007; Vosselman, 2012); however, only a limited number of studies experiment with ALB QC methods (Guenther et al., 2000; Mandlburger et al., 2013; Saylam et al., 2018a; Shin et al., 2016). Because bathymetry - measuring depths and characterizing the bottom topography of inland reservoirs and coastal areas - is a dynamic science field, it is critical to understand and quantify the QC measures that influence the depth accuracies. QC measures are product oriented, and they consist of active processes until project finalization. These measures are concerned with the errors caused by the misalignment of the optical instrumentation and the delays in the electronics such as digitizer latencies for detecting, decoding, and recording the transmitted and received pulses. Further, there are concerns with the pulse energy transit time variations and their respective propagation calculations passing through the air/water interface, and laser output irregularities caused by voltage variations in the aircraft.

Operational errors are caused by mishandling or overlooking of quality assurance (QA) protocols, and these include project activities prior and during data acquisition. They are concerned with underestimating the variable environmental conditions, use of unreliable ground control network, incomplete or inadequate *in-situ* measurements and lacking overall experience and understanding of bathymetric Lidar data acquisition and processing. Although some of these errors can be detected and corrected, undetected errors may cause significant positional inaccuracies that may cause repeat surveys, delays, and project failures. For instance, at a typical ALB survey altitude of 400 meters, a boresight angle bias of 0.05° degrees (less than 1 mrad) would cause 25-cm of height measurement error on the target surface.

Height accuracy of an ALS derived product is reported with statistical methods such as the standard deviation and the root mean square error. Various governing agencies published standards as guidelines to report horizontal and vertical accuracies (Flood, 2004; Kaufmann, 2019). According to the American Society of Photogrammetry and Remote Sensing (ASPRS), the absolute vertical accuracy for DEM products should match or exceed 1.96 times the vertical accuracy class at 95-percentile calculations (ASPRS, 2015). For instance, at 10-cm vertical accuracy class, the non-vegetated vertical accuracy (NVA) should exceed 19.6 cm (95%). Additionally, United States Geological Survey (USGS) published National Map Accuracy Standard (NMAS) and the National Standards for Spatial Data

Accuracy (NSSDA) documents to help understand the accuracy standards [1]. With the NSSDA, the height accuracy of a data set (Accuracy, "*z*") is defined by the RMSE(*z*) of the elevation data in terms of feet or meters of ground scale, rather than in terms of the published map's contour interval. For 1-m contour interval maps, we expect to have vertical accuracy of better than 18.2 cm (0.6 ft.) and RMSE values indicating less than 9.25 cm (0.3 ft.).

According to the International Hydrographic Organization (IHO), standards for ALB surveys are generalized for hydrographic measurements, and do not consider the varying environmental conditions that influence the quality of data. Therefore, in practice, it is a common norm to expect uncertainties with ALB depth accuracies. However, particularly in shallower and relatively transparent waters, ALB depths routinely exceed the *Order 1a* accuracy requirements as set by the IHO (IHO, 2020; Saylam et al., 2018b). In Lower Laguna Madre, the applicable bathymetric standards should be tight due to the nature of the lagoon and the marine vessel traffic that often traverses it. Therefore, BEG applied the *Special-Order* standard for accuracy reporting, which is more demanding and stringent. This standard applies to shallower waters, and it is concerned with the marine vessel underkeel clearance, critical in berthing areas, harbours, areas of fairways and shipping channels.

IHO defines the largest total vertical uncertainty (TVU), where the result is a one-dimensional quantity that includes all contributing vertical uncertainties. The *uncertainty* estimates the range of values within the true value of a measurement and defined within 95% confidence level. In **Equation 6**, *a* is the portion of the uncertainty that does not vary with the depth; *b* is the coefficient which is the part of the uncertainty that varies with the depth; and (*d*) is the measured depth (*a* = 0.25 meters, and *b* = 0.0075). **Table 3** outlines the resulting TVU requirements for IHO Survey *Special Order* at relevant hydrographic survey depths.

$$TVU_{max} = \mp\sqrt{a^2 + (b \times d)^2} \qquad \text{(Equation 6)}$$

Table 3: TVU requirements at certain depths as defined by the International Hydrographic Organization that is applicable to *Special Order* hydrographic standard.

Depth (m)	**1**	**2**	**5**	**10**	**20**
Maximum TVU (± m)	0.25	0.25	0.25	0.26	0.29

[1] USGS Standards and Specifications: https://www.usgs.gov/ngp-standards-and-specifications/standards-and-specifications

i) ALB system calibration

A total of 448 ground control points were acquired over the taxiway surface at Port Isabel-Cameron County, TX airport (KPIL) using a Trimble R8 GNSS receiver. These precise GPS survey points were used to quantify and adjust the slant range biases of Lidar measurements **(Figure 7).** Because NIR and bathymetric scanners function independently, it was important to compute and correct the common offset errors and minimize them. GPS survey points were post-processed to increase their positioning accuracy using TxDOT (Texas Department of Transportation) maintained TXLN (Texas Laguna Madre, 26° 5" 41.6392' N, -97° 18" 02.4998' W) NOAA-CORS (National Oceanic and Atmospheric Administration-Continuously Operating Reference System) base station. The standard deviation for horizontal adjustment was 2.2 cm, and 3.3 cm for vertical adjustment (**Figure 8**). Heights calculated in this practice were ellipsoidal, native, and true to Lidar data acquisition. All ellipsoidal heights were converted to orthometric heights (real world elevations) using the GEOID2012B model to produce the Digital Elevation Models (DEM).

BEG compared ground GPS survey points to the triangulated irregular network (TIN) heights, generated by Lidar returns, using the *least-squares* statistical method (Savitzky and Golay, 1964). Results indicated the goodness-of-fit by computing the R-squared (R^2) value (coefficient of determination), which indicates the percentage of response variable and represents the closeness of the data sets. Additionally, the mean divergence, residuals, and root-mean-square-error (RMSE) values were calculated (**Table 4**). For both scanners, the mean bias and RMSE were less than 3 cm. The correlation between the GPS survey points and the Lidar TIN patch heights produced a high degree of confidence for both scanners ($R^2 > 0.95$, **Figures 9 a, b).** However, findings revealed a slight height discrepancy (< 4 cm) between the scanners, possibly caused by EM energy pulse length and beam divergence differences. This difference is visible in **Figure 10,** where median NIR returns measured surfaces slightly higher (3.8 cm) compared to the green-wavelength scanner measurements**.**

Table 4: Chiroptera Lidar system calibration, slant range (vertical bias) adjustment results.

Scanner type	Number of samples	Data range (m)	Median (m)	RMSE (m)	R^2
NIR	448	0.137	0.025	0.025	0.96
Green	448	0.168	-0.013	0.028	0.95

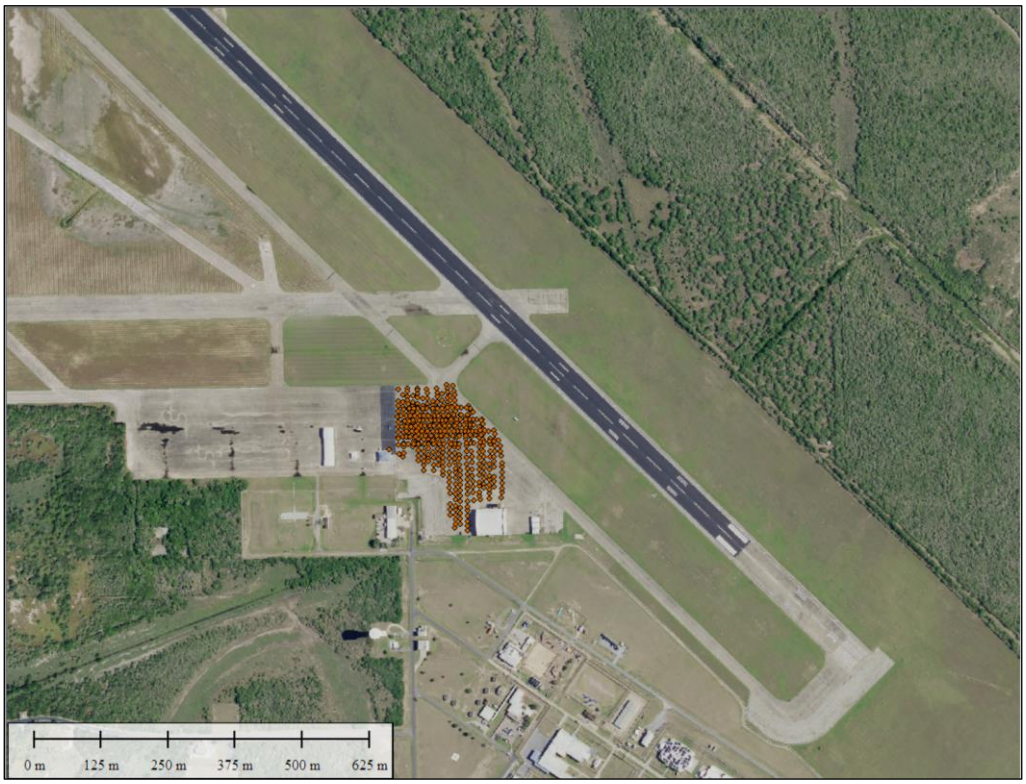

Figure 7: The red dots illustrate 446 GPS survey points acquired using a Trimble R8 GNSS receiver in the taxiway of Port Isabel-Cameron County. Positional measurements were refined by post-processing method using the TxDOT maintained TXLN GPS base station.

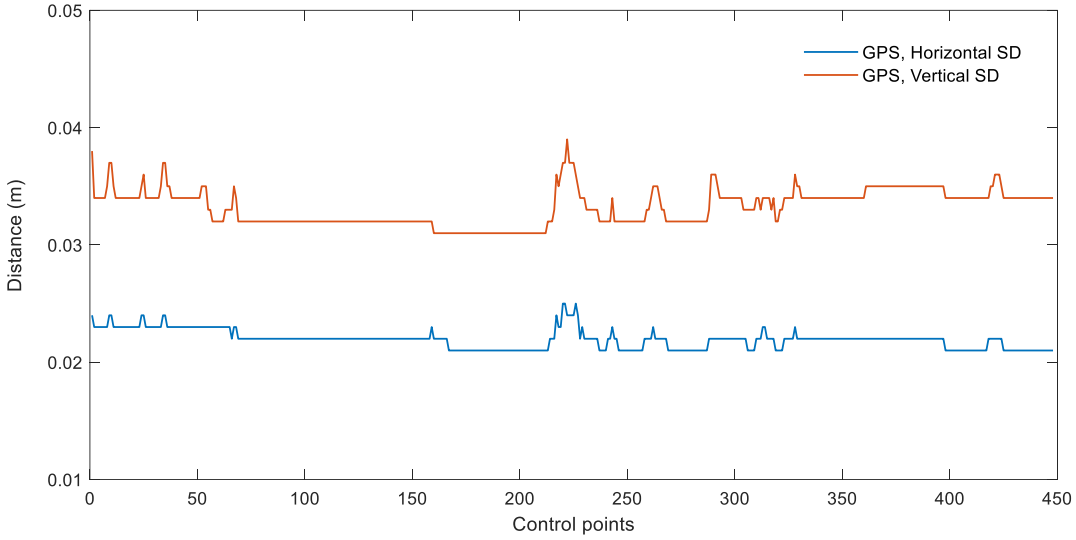

Figure 8: Vertical and horizontal positioning resolution of the static GPS survey points, differentially corrected using the TXLN CORS reference station.

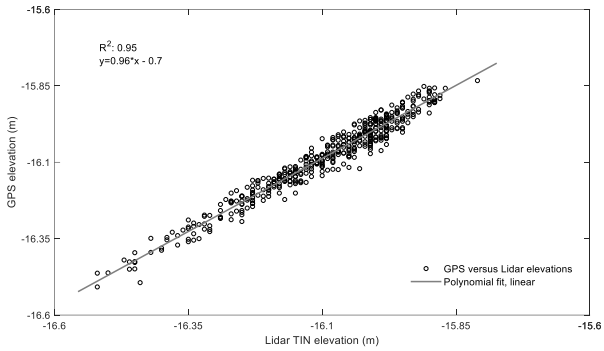

Figure 9 (a): Green-wavelength scanner, vertical height adjustment (GPS survey points versus Lidar TIN patch heights, RMSE=0.028 m, R^2 = 0.95).

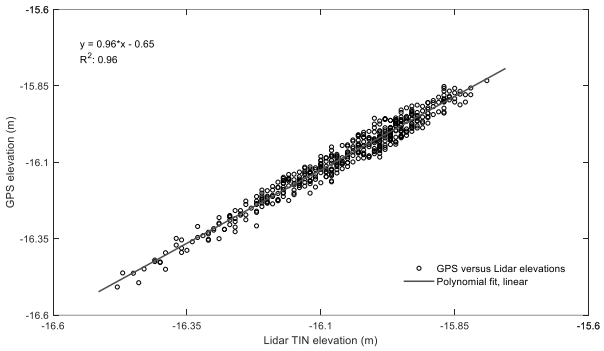

Figure 9 (b): NIR scanner, vertical height adjustment (GPS survey points versus Lidar TIN patch heights, RMSE=0.025m, R^2 = 0.96).

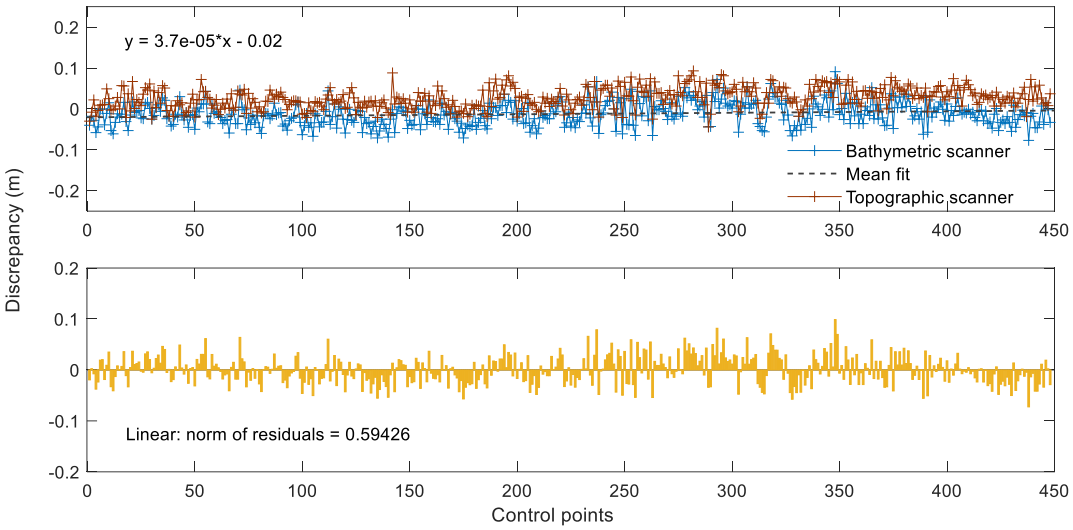

Figure 10: Comparison of slant range adjustment for both scanners. Results indicated a median bias of 3.8 cm between the scanners compared to the Lidar TIN patch heights.

ii) *In-situ* measurements

During data acquisition campaign, BEG conducted *in-situ* measurements that included Secchi disk (S_D) observations and turbidity sampling. Depths were measured using a Garmin sonar at the southern locations of the lagoon, where boat access was feasible (**Figures 11 a, b**). The sonar unit, Garmin 74dv, collected data with single-beam technology (dual frequency) transducer and with an effective depth range of 700 m at 77 kHz. It also sampled positional data at a rate of 5 Hz with a built-in GPS interface. In the lab environment (UT Austin, Advanced Research Laboratories), BEG researchers evaluated the unit to produce depth measurements with standard deviation of 2.7 cm at 11.8 m depth. Because lagoon is large, calm, and shallow, rotational adjustment (attitude) or differential processing for GPS positions were not considered. In deeper and choppier waters, rotational adjustment may be necessary to adjust the depth ranging with the correct angle of scanning.

Figure 11 (a): *In-situ* measurements in Lower Laguna Madre. BEG measured depths using a single-beam Garmin sonar installed onto a kayak.

Figure 11 (b): Researchers measured water quality, transparency, and turbidity in conjunction with the airborne Lidar surveys.

Because of dynamic nature of the lagoon and ongoing tidal effects, surface heights were not expected of high consistency. National Oceanic and Atmospheric Administration (NOAA)[2] reported a daily average of 23 cm tidal elevation variation in Port Isabel gauge (Station ID# 8779770: latitude 26° 3.6', longitude 97° 12.9'), observed in last 19 years. In Port Mansfield (Station ID# 8778490: latitude 26 ° 33.5', longitude 97° 25.5'), solely in May 2017, NOAA recorded 44 cm daily variance (**Figure 12**) and the mean height was 0.19 m MSL. Port Isabel gauge recorded 90 cm of variance for the same period, and the mean height observed was 0.12 m MSL (**Figure 13**). Therefore, especially in the southern parts of the lagoon, greater disparity of tidal effects was expected, influencing the surface heights. The amount of observed tidal influences are presented in **Table 5**, corresponding to sensing time of each satellite image that was used in this study.

As part of the project, additional depth measurements were provided by Texas Commission on Environmental Quality (TCEQ), through the Surface Water Quality Monitoring (SWQM) program. BEG selected five SWQM reference stations that were maintained actively and scattered throughout the lagoon for uniformity (**Table 6**). **Figure 14** illustrates these *reference* station locations (TCEQ IDs: 13446, 13447, 13448, 13449, 14870), and BEG observed *in-situ* locations for depth measurements. There were three areas of clustered *In-situ* locations; Area #1 has shallow and mainly transparent waters, Area#2 has intermittent water quality and depth, and Area#3 has the lowest water quality with deeper sections.

[2] NOAA: Superseded benchmark data sheets: https://tidesandcurrents.noaa.gov/

Table 5: Observed tidal effects at Port Mansfield (ID# 8778490) and Port Isabel (ID# 8779770) stations at 17:00 UTC, corresponding to the satellite imaging acquisition. These observations were used to adjust the depths respective to their bathymetric mapping.

Gauge	**Tidal observation (m)**			
	05/12/2016	06/16/2017	05/17/2018	05/27/2019
Port Mansfield, TX	0.35	0.20	0.15	0.32
Port Isabel, TX	0.53	0.40	0.52	0.46

Table 6: *In-situ* depth measurements used in the SDB analysis, as recorded by TCEQ and BEG. These locations are illustrated on a map, in Figure 14.

Sentinel-2A 1LC imagery	**Sonar / SWQM ID**	**UTM Easting (m)**	**UTM Northing (m)**	**Depth (m)**
2016	TCEQ-13446	680866.0	2892509.6	0.95
2016	sonar	677419.2	2889228.2	1.59
2016	TCEQ-13447	667952.5	2917386.8	0.91
2016	sonar	681075.6	2889328.0	1.22
2017	sonar	682282.8	2890040.0	0.88
2017	sonar	680624.6	2888914.0	0.94
2017	sonar	681989.9	2891306.0	0.74
2017	sonar	681723.8	2891260.0	0.90
2017	sonar	681101.4	2890945.0	0.99
2017	sonar	681434.5	2890731.0	0.91
2017	sonar	681985.0	2890432.0	0.94
2017	TCEQ-13449	652431.3	2963357.0	1.46
2017	TCEQ-13447	667952.5	2917386.8	0.73
2018	Sonar	681075.6	2889328.4	1.22
2018	Sonar	677419.2	2889228.2	1.59
2018	TCEQ-13449	652431.3	2963357.0	0.98
2018	TCEQ-13447	667952.5	2917386.8	1.50
2019	TCEQ-13449	652431.3	2963357.0	1.10
2019	TCEQ-13447	667952.5	2917386.8	1.64
2019	sonar	681075.6	2889328.4	1.22

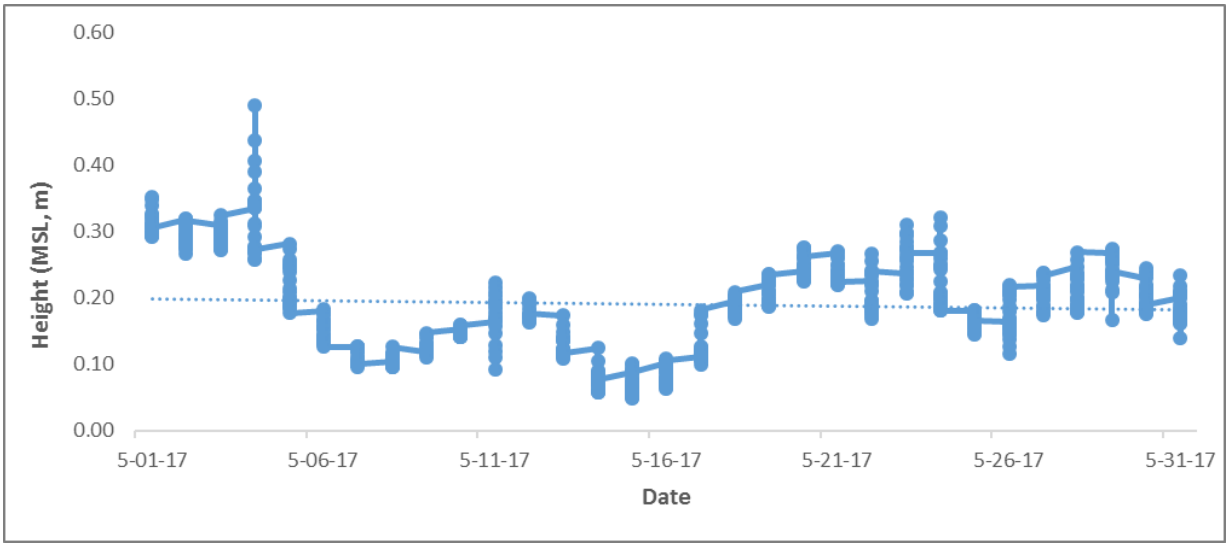

Figure 12: Port Mansfield (ID# 8778490), TX NOAA tidal gauge showing 24-hours of surface height variations. Blue-dashed line indicates the mean tidal height as 0.19 m observed for entire month of May 2017.

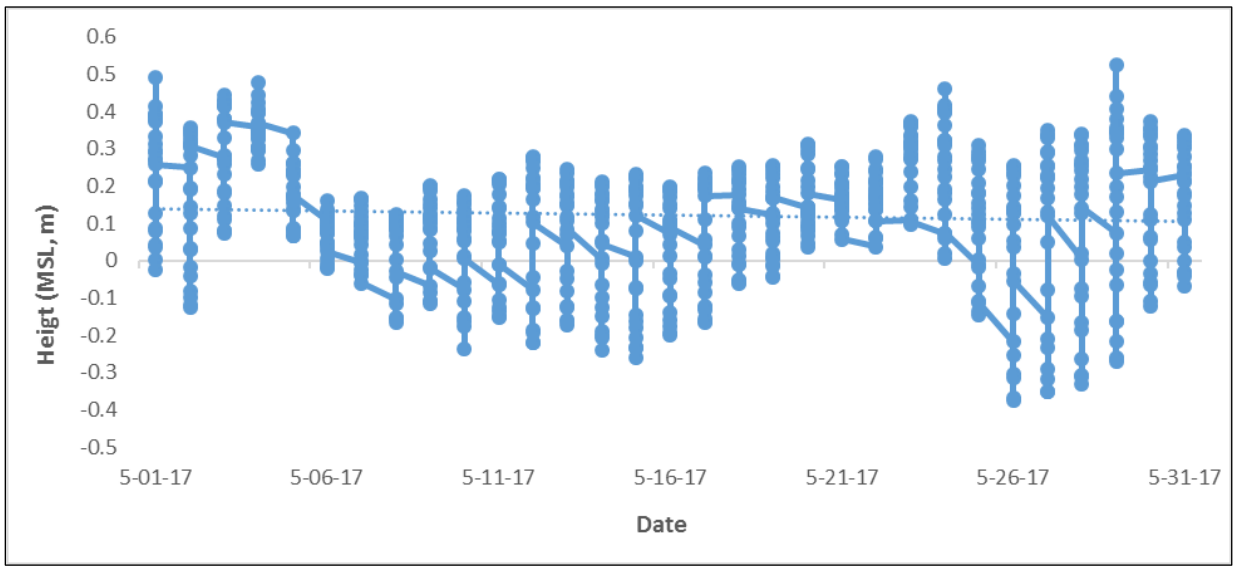

Figure 13**:** Port Isabel (ID# 8779770), TX NOAA tidal gauge showing 24-hours of surface height variations. Mean tidal height observed was 0.12 m for May 2017.

Figure 14: Reference *in-situ* locations (TCEQ-stations and BEG-observations) and sonar depth measurements that were used to analyze satellite imagery. Area #1 (survey date: 05/01/2017) has the lowest and Area #3 (survey date: 05/12/2017) has the highest turbidity content (Appendix B).

iii) Vector data analysis

BEG verified the Lidar bathymetry with sonar and *in-situ* depth measurements (TCEQ and BEG-observed) before comparing the findings to satellite derived bathymetry findings. The varying environmental conditions were expected to have an impact on the quality and completeness of the Lidar measurements. For comparison purposes, with vector data sets, because point-to-point (return) correspondence is not assumed (Habib et al., 2009), the *Delaunay Triangulation* algorithm (B Delaunay, 1932) was used to create surface patches of TIN. There are other algorithms to construct TIN surfaces (e.g. Distance ordering, Region growing); however, because of superior uniform modelling, automation capabilities and statistical consistency with previous QC applications (Saylam et al., 2018b; Zhu et al., 2008), the *Delaunay Triangulation* algorithm was preferred.

A TIN surface is a vector-based model and represents the surface morphology by triangulating a group of points. The surface is constructed from a large network of connecting and non-overlapping triangles. The TIN construction of a Delaunay triangulation follows building of "dual" layer Voronoi diagrams of a given vertex set (**Figure 15 a**). The circumcenters of *Delaunay Triangulation* are the vertices of the Voronoi diagram (**Figure 15 b**). Each vertex of the triangulation is surrounded by a Voronoi cell, which consists of all planar points that are closer to the selected vertex. Two vertices are connected by their edge in the associated *Delaunay Triangulation* if the cells in which the vertices are bordering each other. The algorithm maximizes the smallest angles of triangles in the iteration process by defining an empty circumcircle. **Figure 16 a** illustrates the concept where the algorithm selects the shortest distance of all points (*h*) to minimize the interior angle of all triangles, and the triangles are equiangular.

The vector Lidar data sets were used to construct the TIN surface patches (Surface 1, **Figure 16 b**) by defining a set of circumcircles (e.g., 1 m) and the averaged TIN heights were compared to the heights measured by another survey method (e.g., sonar and GPS) (Surface 2, **Figure 16 c**). The algorithm picks the returns that register in the defined proximity (e.g., *dS1i* = 1 m), and excludes the returns that register at slopes greater than defined (e.g., α=45°) angle. The vertical threshold (e.g., *h* = 0.5 m) is adjusted to prevent the algorithm picking up returns from vegetation or other erroneous features that may represent heights incorrectly.

A text editor (e.g., Notepad++, UltraEdit) and Microsoft Excel were used to organize the vector data sets for analysis with MATLAB R2017b and multiple variations of threshold distances and slope

angles were input to observe optimum results. In more detail, vector data analysis included the following practices:

- Compared the GPS survey points to Lidar measurements and adjusted ALB slant range biases. Analyzed vertical height biases for each of Chiroptera scanners.
- Compared sonar depths to the Lidar bathymetry and investigated the accuracy of the Lidar measurements.
- Compared satellite derived bathymetry in certain *in-situ* locations to Lidar bathymetry and examined the depth differences.
- Prepared statistical results such as standard deviation, mean (average) value and RMSE, and if applicable, the goodness-of-fit between data sets using linear or quadratic regression by producing R-square values (R2) of all comparisons.

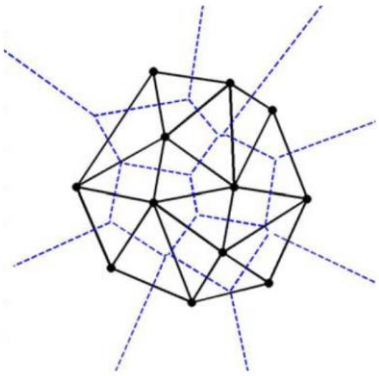

Figure 15 (a): Connecting the centres of the circumcircles to produce the "dual" layer Voronoi diagram (in dashed blue lines).

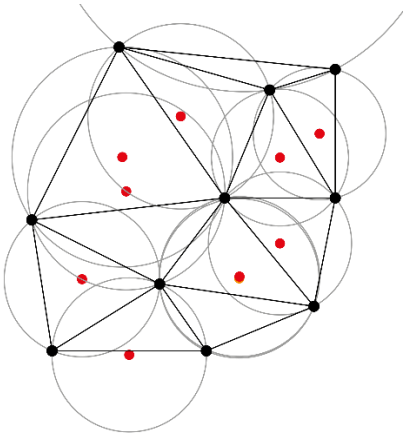

Figure 15 (b): The *Delaunay Triangulation* with all the circumcircles and their centers indicated in red.

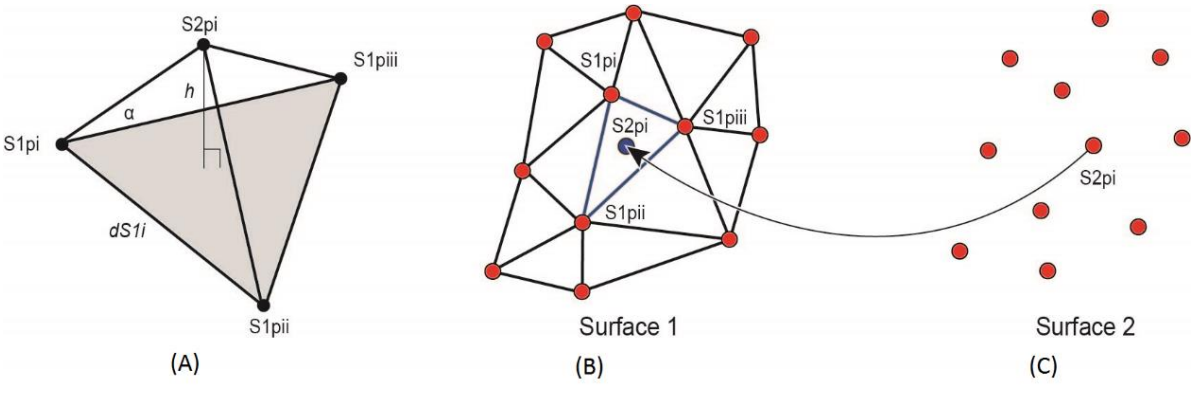

Figures 16 a-c: Conceptual representation of point-to-patch relationship and vector data comparison using the *Delaunay Triangulation* algorithm.

d) Lidar data acquisition

Several airborne campaigns were conducted over Laguna Madre with a Partenavia P68-C (N88N) fixed-wing aircraft (**Figures 17 a, b**). Data acquisition campaign was tedious and challenging because of intermittent weather and tidal conditions that influenced the depth, water quality and surface choppiness. An area of approximately 1,600 km^2 were covered that included bank-to-bank channel bathymetry of the lagoon (Sections B and D), South Padre Island shoreline (~200 m into the Gulf Coast, Section E), the immediate lagoon topography (Sections C and D), and the southerly-located inland water reservoirs (Section F). **Table 7** provides a summary of Chiroptera settings used during airborne survey missions; and **Appendix A** provides a detailed day-by-day data acquisition information and **Figure Appendix A-1** illustrates the survey sections. In conjunction with ALB data acquisition, BEG conducted *in-situ* campaigns to quantify the water quality, transparency, and depths in the southern part of the lagoon, where the boat access was granted and feasible **(Appendix B)**.

Table 7: Chiroptera system settings used for Lidar data acquisition in Lower Laguna Madre survey.

Item	**NIR wavelength**	**Green wavelength**
Pulse repetition rate	100-300 kHz	36 kHz
Survey altitude (AGL)	400-600 m	
Lidar swath and overlap	250-300 m / 30% overlap	
Aircraft survey speed	110-130 knots	
Camera overlap	20% forward, 30% side	
Camera filter and GSD	Natural colour (RGB) / 6 cm/pixel	
Lidar point density	10 points/m^2 (+side overlap)	2 points/m^2 (+side overlap)

Figure 17 (a): Partenavia P68-C (N88N) in Port Isabel, TX airport.

Figure 17 (b): BEG researchers are installing the AHAB Chiroptera Lidar system and other required equipment in the Partenavia P68-C aircraft.

e) Satellite imaging analysis

i) Imagery downloads and preparation

Satellites with high-resolution imaging sensors can cover large areas with detail, allowing visualization of various features. In this project, BEG researchers downloaded archived imagery from the Planet Explorer online database[3]. The database enables searching and downloading of archival imagery and contains a multitude of high-resolution data acquired by various sensors, supplying a global coverage. Because Laguna Madre is a dynamic estuary, and airborne Lidar data sets were acquired in May and June, for temporal study and consistency purposes, researchers downloaded imagery solely acquired in May and June of 2016-2019. Because of several *in-situ* measurements were blocked by clouds, 2020 imagery were excluded.

The European Space Agency (ESA) owns and operates the Sentinel-series satellites and currently manages two satellites in the orbit: Sentinel-2A and 2B. These satellites complete a full orbital cycle at every 10 days, and they acquire imagery to support the various industries and applications such as agricultural monitoring, emergency and disaster management, land cover classification and water

[3] Planet Explorer: https://www.planet.com/

quality monitoring. Sentinel-2A's multispectral image sensor captures and records target surfaces with 13 spectral bands. Depending on the wavelength, these bands have a spatial resolution of 10, 20 and 60 m. The payload data ground segment (PDGS) processes Level-1C (L1C) products and outputs radiometrically and geometrically corrected top of atmosphere (TOA) multispectral images. L1C products are composed of 100 x 100 km^2 tiles, and they include cloud masks and European Centre for Medium Range Weather Forecasts (ECMWF) information (total column of ozone, total column of water vapour and mean sea level pressure). Every L1C product contains information with wavelength bands 1 to 8A (442.7 to 864.7 nm). In this study, Bands 4, 5 and 8 were essential because of their capability to prevail differences in reflectance values among water and terrain, emphasizing the vegetation boundary between land and water (Mondejar and Tongco, 2019). The sampling resolution varies with each band, 10-20 m per pixel for the Bands 4-8A. Acquisition time, date, tile numbering, ground sampling resolution and other specifics of the downloaded imagery are provided in **Table 8.**

Table 8: Details of Sentinel-2A L1C images used in the Lower Laguna Madre study.

Date	Sensing Time (UTC)	Tile	Sun elevation (degrees)	Sun azimuth (degrees)	Cloud coverage (%)
12/05/2016	17:11:44	T14RPQ	72	113.6	20
12/05/2016	17:11:44	T14RPP	72.3	111.1	24
16/06/2017	17:15:05	T14RPQ	72.9	96.9	6
16/06/2017	17:15:05	T14RPP	73	94	6
17/05/2018	17:10:16	T14RPQ	72.4	110.5	0
17/05/2018	17:10:16	T14RPP	72.8	107.9	0
27/05/2019	17:16:29	T14RPQ	73.1	104.5	25
27/05/2019	17:16:43	T14RPP	73.3	101.6	16

In sequence, BEG performed the following steps to download and process satellite imagery of Laguna Madre:

- Investigated and determined that Sentinel-2 products suited the project requirements because of their spatial resolution, lower cloud coverage and higher temporal variability compared to other imagery available (e.g., RapidEye, Landsat-8).
- Verified that Sentinel 2- L1C products do not require additional radiometric calibration, images are calibrated at top of the atmosphere.

- Mounted a temporal constraint in the Planet Explorer query screen to determine the most viable data sets (e.g., free of clouds, atmospheric distortions) and selected suitable imagery of the lagoon.
- Downloaded two tiled imageries for each year to capture the entire lagoon, with Bands 1-8A (tiles T14RPQ and T14RPP) and verified the meta data and georeferencing information for further suitability in the study,
- Used ENVI v5.5 Layer Stacking Tool to layer Bands 1-8A. This tool manipulates bands from georeferenced images of diverse sizes and re-projects the bands to a standard spatial grid to produce one multi-band file.
- Used ENVI's Seamless Mosaic workflow to piece together the two tiles into one image.
- Mounted the mosaic data set into ENVI's Subset Data from Region of Interest (ROI). A shapefile of the Laguna Madre ROI was created in Google Earth, then uploaded into ENVI v5.5.
- Applied an additional spatial constraint to mosaicked tiles to exclude surrounding land and manufactured features to emphasis on the water body.

ii) Reflectance

Analysis of EM radiation (reflectance) recorded of target surfaces may supply essential information about the water depth, water quality, and other surface properties. The visible and NIR spectral wavelengths can distinguish the varying concentration of suspended particulate matter in the water (Gernez et al., 2015). According to Sebastiá-Frasquet et al. (2019), using the Sentinel-2A L1C Band 5 (705 nm), it is possible to estimate the water quality within 20 m of spatial resolution in shallow lagoons with average depth of 1 m, which is similar to Laguna Madre depths.

ENVI v5.5 Spectral Profile Tool was used to analyze the radiance recorded at each pixel to predict the surface reflectance. The principal purpose was to predict the water quality and its influence on Lidar and satellite bathymetry; however, the reflectance values of each pixel helped us to determine the nature of the surface analyzed (e.g., vegetation, high or low water quality) and we were able to generate polygon masks separating the lower reflectance areas for mounting into ENVI's SPEAR satellite derived bathymetry (SDB) analysis tool. The areas where the reflectance values represented cloud coverage, which produced a greater value compared to cloud free locations were removed. Further, five refence locations were selected (maintained by TCEQ) that were visible by all imagery and mounted these locations to ENVI Spectral Profile tool to analyze the radiance recorded by Band 4 (665 nm) and

Band 5 (705 nm). The purpose was to investigate the spectral radiance differences at the same location with each year's imagery. These reference locations are illustrated previously in Section 2-h (**Figures 15 a-d)**.

To plot the reflectance analysis results, ENVI's Iterative Self Organizing Data Analysis (ISODATA) clustering algorithm was used. This is an unsupervised classification tool that iteratively clusters pixels to the nearest class with relatively good accuracy (Ahmad and Sufahani, 2012). The algorithm does not require *a priori* knowledge of the surfaces and continuously computes the mean values by reclassifying the pixels until the alteration between the pixels is less than the set threshold (2%) or the maximum number of iterations (default, 10) is achieved.

Further, a Normalized Difference Water Index (NDWI = (green-NIR)/(green + NIR)) analysis was conducted to build a surface map by mounting the areas of interest, using the green and NIR bands (Wang et al., 2019). Typically, NDWI analysis can detect moisture changes in the vegetation (Gao, 1996), and in this study, the formulae was used to exclude cloudy and vegetated areas as identified by the ISODATA analysis. The band reflectance was normalized (0-1) using the ENVI Band Math tool's recommended reflectance multiplicative band scaling factor. The scaling factor normalizes the images to reduce radiometric differences across multi-temporal imagery from non-surface effects (de Carvalho et al., 2013).

iii) Bathymetry

Satellite derived bathymetry concept includes active and passive spaceborne sensors to map the shallow water habitats. In this study, SDB stands for passive, optical-imaging based bathymetric analysis.

Water-leaving radiance is the backscatter upwelling after traversing the air/water interface and recording subsurface volumetric and water bottom information. Accurate estimates of water depth with optical-imaging can be limited by numerous factors such as atmospheric influences, water quality and depth. Previous studies indicated that Band 4 (665 nm) can distinguish the chlorophyll-A maximum absorption, and Band 5 (705 nm) relates to the vegetation monitoring and turbidity patterns in shallow lagoons (Delegido et al., 2011; Sebastiá-Frasquet et al., 2019). For the purposes of optical-imaging bathymetry, Stumpf et al. (2003), developed the bottom albedo-independent bathymetric algorithm that distinguishes different bottom types such as sand, rock and vegetation with an effective mapping up to 15 meters in ideal atmospheric and water conditions (Favoretto et al., 2017).

The Spectral Processing Exploitation and Analysis Resource (SPEAR) algorithm in Relative Water Depth tool in ENVI v5.5 allows analysts to predict water depths using passive SDB and relevant photogrammetric methods. The algorithm requires the visible (blue, green, red) and NIR bands; which correspond to Sentinel-2 bands 2, 3, 4, and 8A. According to Darama et al. (2019), SPEAR algorithm can distinguish bottoms (vegetation versus sand) at the same depth. *In-situ* depth measurements were needed to generate absolute results (**Table 6**) when subset regions were created by the SPEAR algorithm. Depths produced by SPEAR algorithm were compared to Lidar bathymetry to quantify the accuracy and useability for chart mapping of the lagoon.

3) On-site analysis

In 2017, BEG researchers conducted data processing activities in the field, immediately after completing each data acquisition campaign. Because bathymetric Lidar data processing is significantly different and complicated compared to the NIR data processing, decimated vector data sets were output to verify coverage and depth measurements. In Laguna Madre, survey area included varying terrain (dunes, inland water reservoirs, vegetation, mudholes and manufactured structures) and the lagoon water differed in clarity and depth. Ongoing tidal conditions and shifting high winds affected the surface heights and the absolute depths.

On site, BEG processed three types of airborne Lidar data sets: water surface, bottom, and topography. For *water surface indication*, Lidar Survey Suite (LSS v2.4) algorithm produced two classes of bathymetric data sets; Class 0 combines NIR and green-wavelength returns, and Class 5 is derived solely from the green-wavelength. For depth measuring, LSS algorithm output returns with distinctive peaks as Class 7 (standard) and classifies returns with less significant peaks as Class 10 (enhanced). AHAB developed the enhanced algorithm to increase the depth measuring capability by filtering the weaker bottom return peaks created by low or moderate levels of turbidity.

Previously, in the Colorado River study (Saylam et al., 2017b), where water was deeper (up to 10 m) and relatively transparent, BEG observed depth measuring capability to increase by a smaller margin (9.2%) using the enhanced depth classification algorithm. In Laguna Madre, BEG measured varying turbidity content where *in-situ* measurements were conducted (**Appendix B**). Analysis showed substantial increase in depth measuring capability (up to 41%, **Table 9**) where water was shallower than

2 meters. The bottom was visible at all sampling locations in Area #1; however, Areas #2 and #3 had lesser transparency due to the increased levels of turbidity (**Figures 18 a, b**)**.** On-site analysis indicated a reduced correlation between Classes 5 and 7 with increasing turbidity content (**Table 10**). Naturally, escalating levels of turbidity scattered the light beams, producing a less reliable surface representation.

Table 9: Water-bottom output (Class 7 and 10) comparison to sonar depths at BEG-observed *in-situ* locations.

Area	Number of returns (Class 7 / 10)	Mean sonar depth (m)	Mean Lidar depth (m) (Class 7 / 10)	SD (m) (Class 7 /10)	Depth measuring improvement (%)
1	256 / 130	1.40	1.28 / 1.57	0.14 / 0.23	23
2	381 / 140	1.43	1.42 / 1.75	0.17 / 0.27	20.2
3	551 / 272	1.84	1.3 / 1.84	0.62 / 0.63	41.2

Table 10: Average turbidity and water-surface output (Class 0 and 5) comparison. Increasing turbidity levels impacted the correlation and QC algorithm produced fewer correlation.

Area	Mean turbidity (NTU)	Number of returns (Class 0 / 5)	Median difference (m) (Class 0 to 5)	RMSE (m) (Class 0 to 5)	R^2
1	2.7	528 / 173	-0.07	0.03	0.936
2	8.6	907 / 653	-0.09	0.06	0.651
3	10.5	806 / 420	-0.11	0.08	0.319

Figure 18 (a): Transparent and shallow area, aerial imagery (Area #1). Bottom properties are clearly visible (mix of vegetation and sand).

Figure 18 (b): High turbidity with horizontal floating vegetation as captured by aerial photography (Area #3).

4) Results

a) Reflectance

Six ISODATA classes of reflectivity (low, mixed, moderate-low, moderate-high, high and unclassified / cloud) were generated as an output of the Sentinel-2A 1LC 2016, 2017, 2018 and 2019 imagery, which was in line with the Alaskan North Slope study (Saylam et al., 2017a). The classifications were based on 2% of spectral variance between the recorded values and results omitted high turbidity and unclassified/cloud areas to generate the masking polygons. **Tables 11 and 12** present the reflectance values recorded at selected TCEQ *reference* stations and **Figure 19** illustrate the average reflectance values recorded at these locations. **Table 13** provides the pixel count percentages of each image because of ISODATA classification.

The final ISODATA classifications and corresponding maps were produced in raster format (GeoTIFF) using ArcMap 10.8.1 (**Figures 20 a-d, Appendix C, Figures C-1 to C-4**). The reflectance maps demonstrate the dynamic nature of the lagoon by indicating the variations in the surface water quality. Following statements can be assumed by examining the findings:

- In 2016, the average reflectance values (Bands 4 and 5) were the lowest, therefore, the overall surface water quality was higher.
- In 2016, the moderate-high and high reflectance classes indicated the lowest pixel counts (3.54%), confirming higher water transparency and quality, particularly in the southwestern parts of the lagoon.
- In 2017, the low reflectance classes were least significant (1.05%) while the mixed reflectance class registered (6.02%) the most substantial.
- In 2018, turbidity concentration was higher, leading to lower pixel count in moderate-high and high reflectance classes (5.22%). Overall water quality has increased visibly in the northern parts of the lagoon.
- In 2019, the low reflectance class registered the highest pixel count (4.33%), resulting in the most suitable conditions for satellite bathymetry.

Table 11: Surface reflectance values (0-1) registered with Sentinel-2A L1C Band 4 (665 nm) at TCEQ maintained *in-situ* locations. "N/A" indicates cloud coverage.

***In-situ* location, TCEQ ID**	**Recorded reflectance (0-1) Band 4**					
	2016	**2017**	**2018**	**2019**	**Average**	**Standard Deviation**
1-13449	N/A	0.112	0.111	0.133	0.119	0.012
2-13448	0.123	0.134	0.143	0.145	0.136	0.010
3-13447	0.138	0.117	0.122	0.111	0.122	0.011
4-14870	0.151	N/A	0.136	0.171	0.153	0.017
5-13446	0.159	0.144	0.117	N/A	0.140	0.021

Table 12: Surface reflectance values (0-1) registered with Sentinel-2A L1C Band 5 (705 nm) over TCEQ provided *in-situ* locations, 2016-2020. "N/A" indicates cloud coverage.

***In-situ* location, TCEQ ID**	**Recorded reflectance (0-1) Band 5**					
	2016	**2017**	**2018**	**2019**	**Average**	**Standard Deviation**
1-13449	N/A	0.098	0.096	0.122	0.106	0.015
2-13448	0.111	0.115	0.128	0.134	0.122	0.010
3-13447	0.131	0.118	0.127	0.114	0.123	0.008
4-14870	0.136	N/A	0.116	0.149	0.134	0.017
5-13446	0.138	0.122	0.103	N/A	0.121	0.018

Table 13: Pixel count in percentages (%) of each imagery as classified by ENVI's ISODATA algorithm. "N/A" indicates the areas outside the lagoon.

Imagery	Reflectance pixel count (%)						
	Low	Mixed	Moderate-low	Moderate-high	High	Unclassified/ Cloud	N/A
2016	4.16	5.79	6.11	2.97	0.58	0.09	80.31
2017	1.05	6.02	5.58	3.18	1.05	0.04	83.07
2018	3.94	5.68	5.51	4.08	1.14	0.14	79.50
2019	4.33	4.91	5.37	2.66	1.18	0.09	81.47

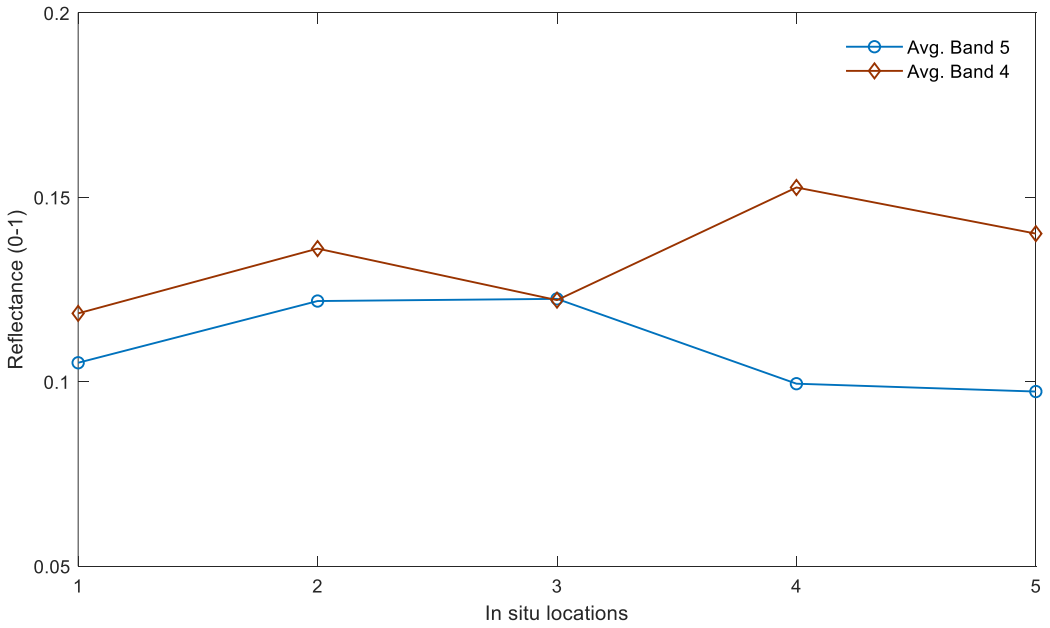

Figure 19: 2016-2019 Sentinel-2A L1C, Bands 4 and 5, reflectance recorded at *in-situ* locations (1-5, TCEQ).

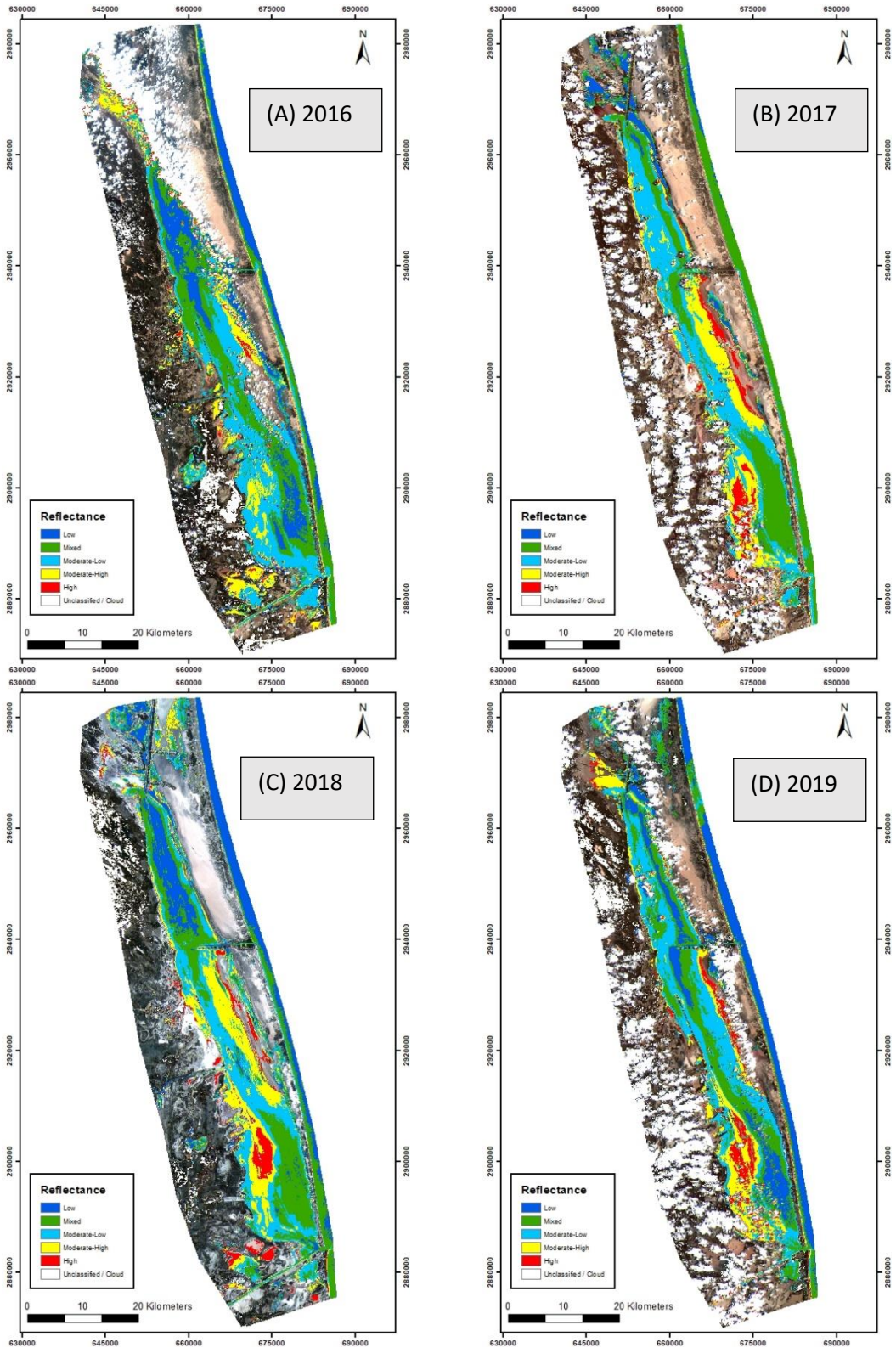

Figures 20 a-d: Reflectance analysis as recorded with Sentinel-2A L1C Band 5, classified using ENVI v5.5 ISODATA algorithm (Maps: **Appendix C**).

f) Lidar bathymetry

In this study, Lidar bathymetry data sets are tiled and delivered in 2x2 km files for visualization simplicity and data management purposes. GPS (ellipsoidal) heights were converted into real world (orthometric) elevations and depths were output in metric units, excluding the areas that registered above 0-meters. **Figure 21** is the north end of the lagoon, illustrating the water bottom details, where Lidar bathymetry is draped over 60-cm National Agriculture Imagery Program (NAIP) imagery. The figure includes the template that demonstrates the UTM location of each tiled data set respective to its northeastern corner.

Because of the dynamic nature of the lagoon and its diverse morphology, varying levels of water quality, tidal influence and surface choppiness influenced ALB depth measuring performance, especially at southwestern and northern sections. At certain locations, ALB was not able to measure the bottom of the lagoon; therefore, BEG suggested TWDB to outsource hydrographic surveying to measure bottoms of missing sections (e.g., southwest lagoon) using multi-beam sonar. **Figure 22** illustrates three sections of the lagoon with low water quality that affected depth mapping using ALB.

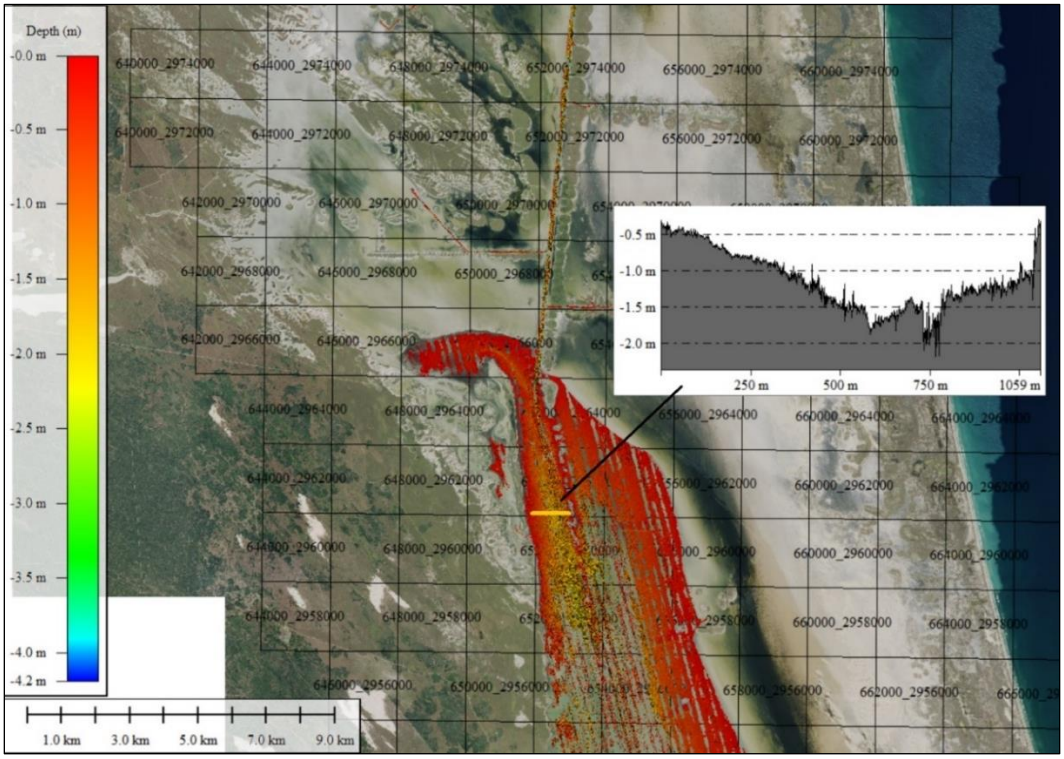

Figure 21: Depth illustration in the north end of the lagoon. Lidar bathymetry draped over 60cm GSD NAIP imagery and grid tiling template.

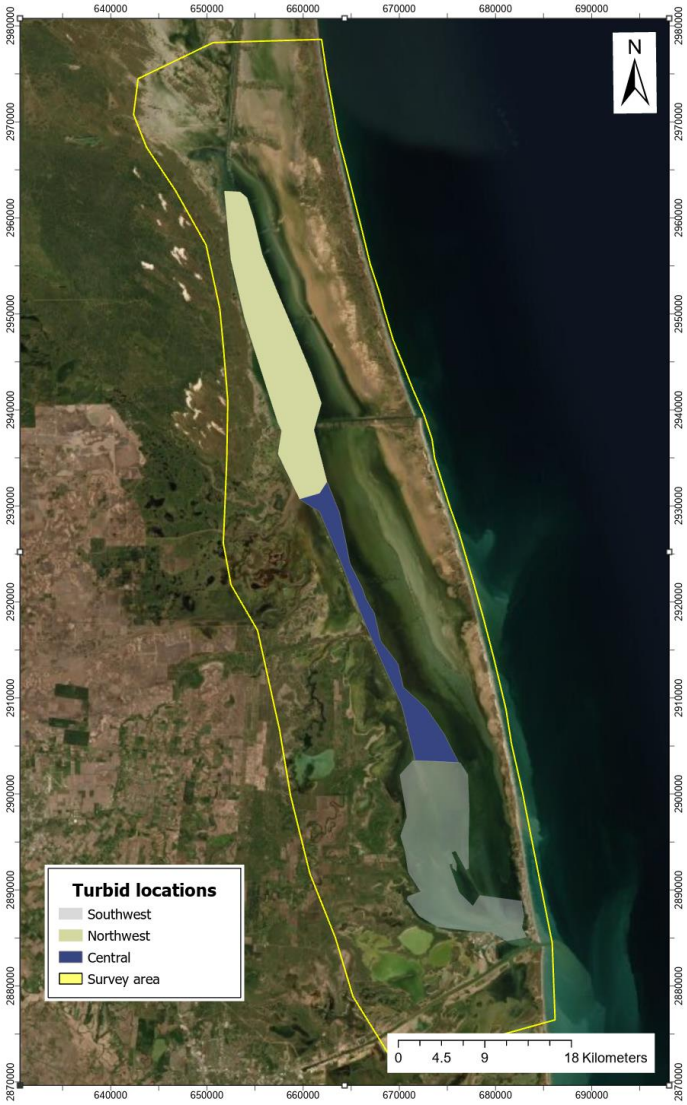

Figure 22: Sections of Lower Laguna Madre with higher turbidity concentration in May 2017. These sections were suggested for sonar mapping to build a complete hydrographic mapping of the lagoon.

Prior to comparing Lidar bathymetry to sonar depths, sonar measurements were adjusted with observed tidal heights using the gauge in Port Isabel. For instance, the gauge recorded 0.39 m surface height variance during the sonar survey conducted at 05/01/2017, 0.31 m in 05/05/2017, and 0.52 m in 05/12/2017. In this analysis, because of their better depth performance, Class 10 data sets were used. Findings indicated that Lidar measured deeper in areas with higher water quality (Area #1), and sonar recorded deeper at turbid areas (Area #2), which was an expected result (**Table 14**). Further comparison of Lidar bathymetry to sonar depths using the QC algorithm revealed robust results, and overall, the

depth accuracies exceeded the *Special-Order* standards set by IHO (TVU < 0.26 m, shallower than 10 m). The QC findings reflected a polynomial fit because the least-squares method minimized the variance of the unbiased estimators of the coefficients, under the conditions of the Gauss-Markov theorem (Shaffer, 1991). Further, we can accept the following statements:

- In Area#1, initially, the QC algorithm returned poor correlation efficiency of 26% (1688/6391) matching sonar depths to Lidar bathymetry. The distance of circumcenter triangle coverage (default *dS1i* = 1 m) of Lidar TIN patches was adjusted to 2 m, height (dZ) tolerance to 25 cm (default=10 cm) and the slope angle was decreased (default=45°) to 30-degrees. As a result, the algorithm efficiency increased, and the matching rate improved (80%). At Area #1, where water column is shallow (mean depth < 1 m) and relatively transparent (mean turbidity=2.7 NTU), the average depths for Lidar/sonar were 0.94/0.9 m and the deepest location was 1.96 m (**Figure 23**).
- In Area#2, where turbidity level increased (mean turbidity = 8.6 NTU), the QC algorithm matched fewer sonar depths to Lidar bathymetry (39%). The mean ALB was 1.02 m and mean sonar depth was 8 cm deeper (1.10 m). The regression result was considerably poor (R^2 =0.34).
- In Area#3, where poor water quality was observed (mean turbidity=10.5 NTU), Lidar returns were scattered, and amplitudes were not sufficient to measure the lagoon bottom. With default parameters, the QC algorithm produced unreliable results; therefore, tighter distance values were input to include only legitimate returns. Expectantly, the correlation efficiency dropped to 20%, increasing the regression result (R^2=0.78). Median ALB was 1.05 m, where sonar measured deeper at 1.23 m (**Figure 24**).

Table 14: Sonar depths versus Lidar bathymetry (Class 10) comparison at different *in-situ* locations.

Location	Tidal adjustment (m)	Mean turbidity (NTU)	Algorithm triangle (m)/ dZ tolerance (m)/ slope (degree)	Matching (%)	Difference (Lidar-sonar, m)	RMSE (m)	R^2
Area 1	0.39	2.7	2/0.25/30	80	0.04	0.15	0.69
Area 2	0.31	8.6	2/0.25/30	39	-0.08	0.15	0.34
Area 3	0.52	10.5	1/0.5/30	20	-0.18	0.21	0.78

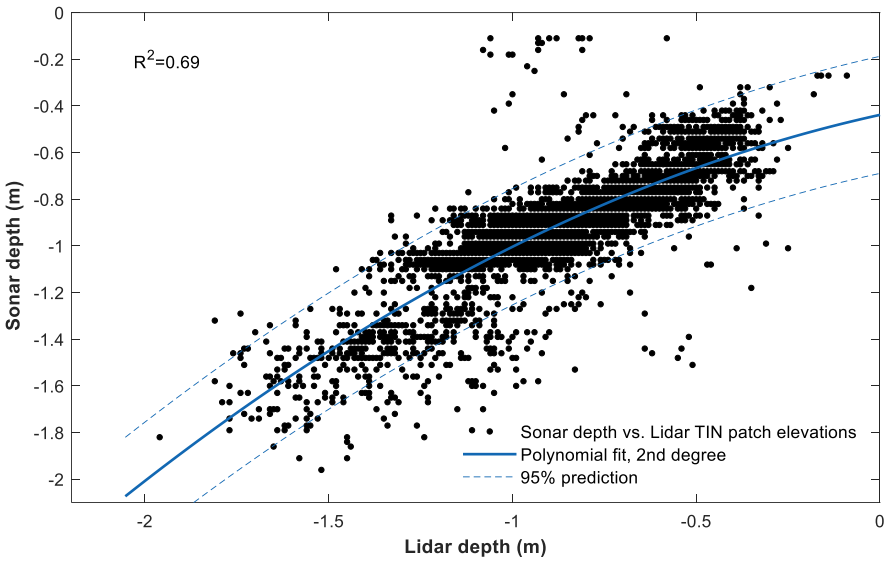

Figure 23: In Area #1, the relationship between ALB and sonar depths produced a 2nd-degree polynomial linear regression (R^2=0.69), which is indicative of increasing noise in deeper water column. Lidar measurements were slightly deeper and mean difference was 4 cm.

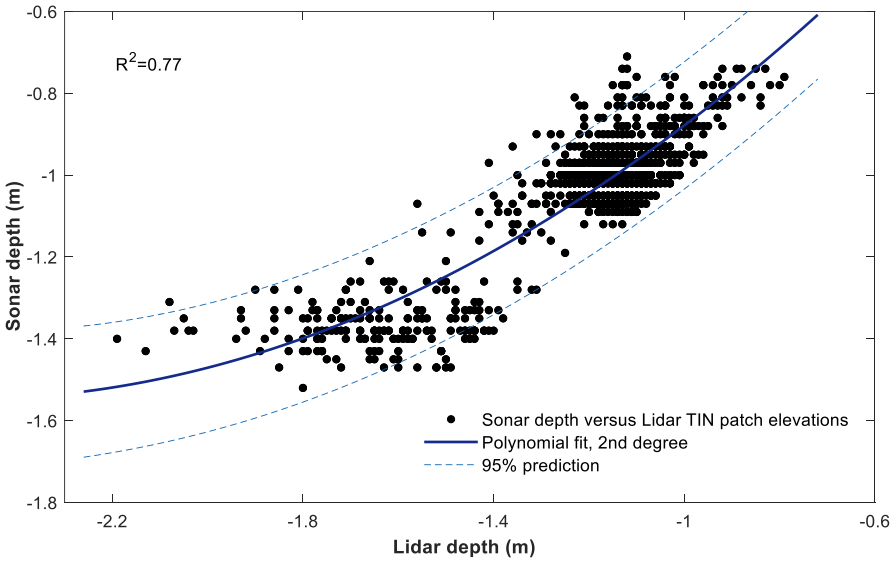

Figure 24: In Area #3, variable and higher turbidity levels were observed that scattered the Lidar returns. QC algorithm matched fewer measurements (20%) because of tighter thresholds. The mean difference increased to 18 cm; however, the regression improved (R^2=0.78).

BEG researchers output vector Lidar surface data sets (Class 0: NIR and green wavelength returns) and created DEM of the lagoon (1-m grid sampling) to visualize the water surface height differences occurred naturally during the data acquisition campaign. The purpose of providing surface

ALB data sets is to illustrate the tidal influences that impacted the water column depths and inform hydrographic analysts to calculate the locational depths. The accuracy of measuring the bottoms is not impacted by the tides, rather the depths. In this study, ALB surface data sets revealed surface height differences of 0.84 m (lowest=-0.28 m, highest= 0.56 m). The mean surface height was 0.04 m, and standard deviation was 0.18 m throughout the airborne survey duration. Findings were in line with 0.9 m tidal influence that was observed at Port Isabel gauge, in May 2017. Especially in the southeastern sections of the lagoon, tides were prevalent, and influenced the overall bathymetric mapping efforts (**Figure 25**).

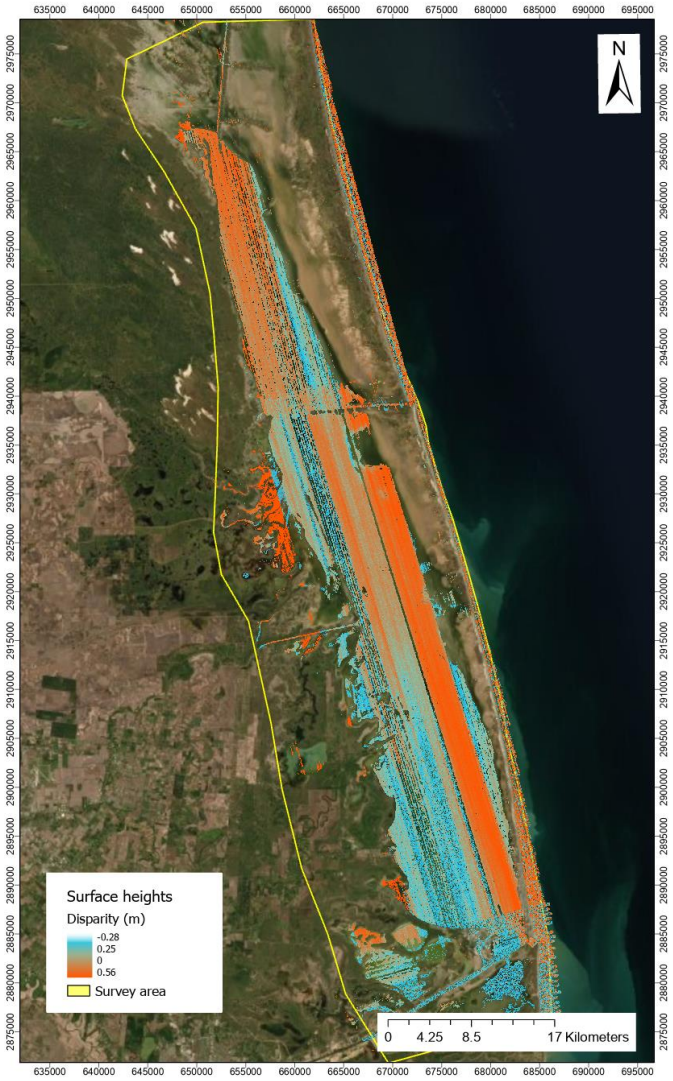

Figure 25: Water surface heights difference because of tidal influences. The mean surface height was 0.04 m, and standard deviation of 0.18 m for all surface height measurements.

For the lagoon depths and bottom representation, ALB data sets were output in three separate classes: Class 6 for shallow and immediate returns, Class 7 for 'regular' bathymetric returns and Class 10 for 'enhanced' bathymetric returns. In this study, BEG provided ALB data sets in whole, and with separate data classes, and each class representing varying properties of the water surface and the bottom. For instance, Class 10 classification algorithm picks a weaker peak in the waveform as the return where it was omitted by Class 7 algorithm since the amplitude registered lower than threshold because of excessive turbidity or depths. Class 6 returns are not reliably indicative of bottoms, so they were not used in the depth assessment.

Analysis of ALB data sets revealed that *in-situ* areas differ slightly in-depth characteristics (Table 15). Area#1 registered the deepest location, and Area#2 had greater average depth. Because of lesser water quality, in Area#3, 28% of all depths were shallower than 30 cm, which caused Lidar beams to scatter immediately beneath the surface (**Figures 26 a-c**).

Chiroptera measured the lagoon at deepest 4.25 m (UTM N 663160, E 2971873; N 668825, E 2949235) and the depths excluded from computations where heights were greater than -0.01 m. Lidar bathymetry indicated the mean depth of the lagoon at no more than 0.61 m, where 48% of all depths were shallower than 0.4 m, and only 1.07% of measurements were deeper than 2.88 m (**Figure 26-d**). However, this may not represent the true lagoon depths because of the limitations of ALB technology in varying environmental conditions. Particularly in moderate-turbid locations, Lidar beams penetrated the water-column slightly, and returned to the receiver immediately before they attenuated, registering very shallow depths that may not reflect actual depth. However, depths measured greater than 0.4 m (> 51%) have higher probability to be accurate and represented the actual lagoon bottom. **Figure 27** presents the bathymetry of entire lagoon, where ALB technology was successful to map the bottom particularly in the northeast and southwest sections.

Table 15: ALB analysis results of *in-situ* areas and the entire lagoon.

Location	Raster cell size (m)	Minimum depth (m)	Maximum depth (m)	Mean depth (m)	SD (m)
Area#1	1	0.01	3.35	0.86	0.25
Area#2	1	0.01	3.31	1.12	0.27
Area#3	1	0.01	2.93	0.90	0.58
Laguna Madre	1	0.01	4.25	0.61	0.67

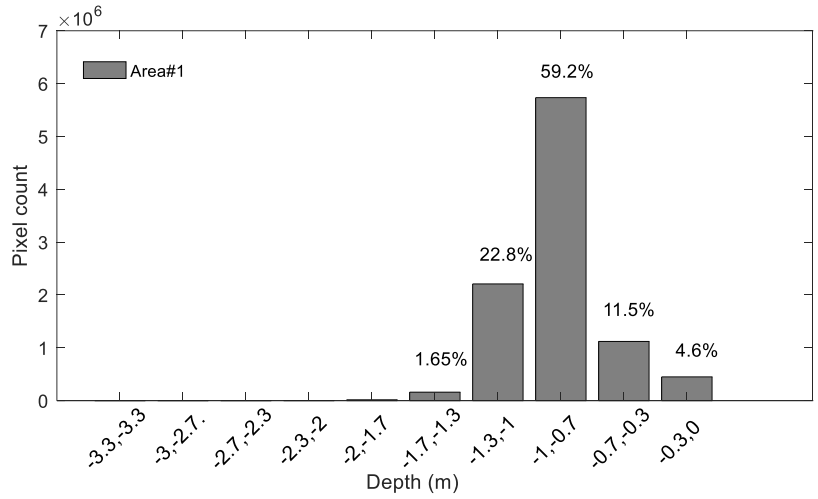

Figure 26-a: Area#1, ALB results. The deepest area was 3.35 m, and the average depth was 0.9 m. 24% of depths were greater than 1 m.

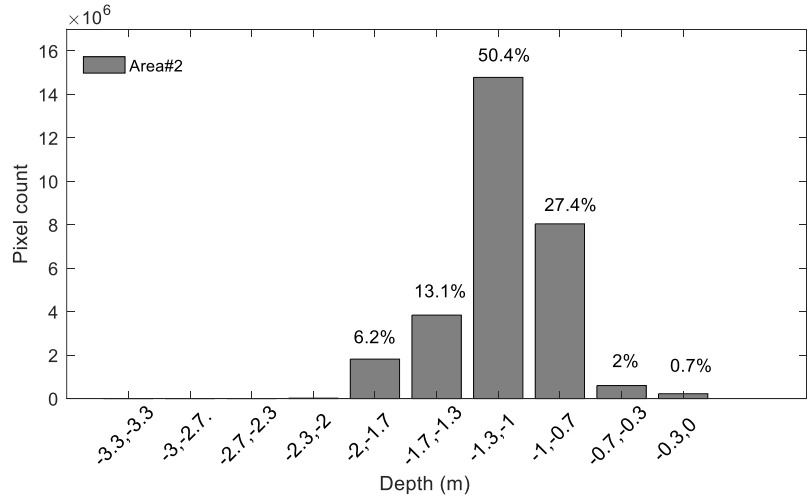

Figure 26-b: Area#2, ALB results. Average depth was 1.12 m and 69% of all measurements were deeper than 1 m.

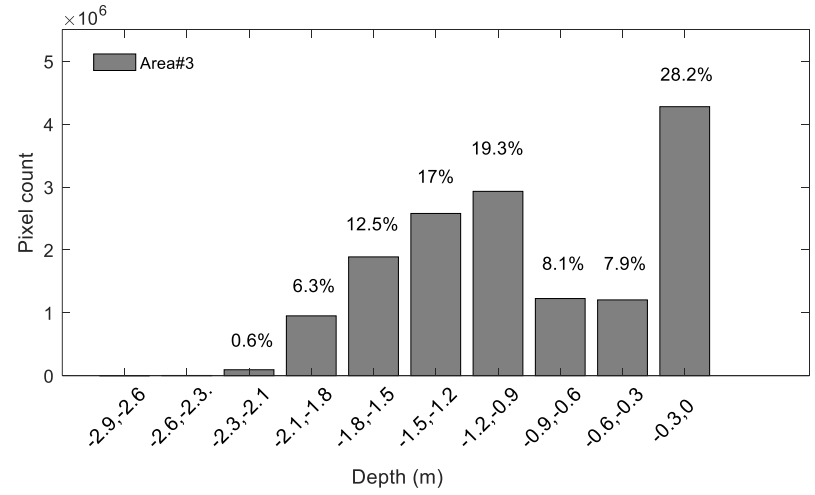

Figure 26-c: Area#3, ALB results. Depth measures were impacted by the poor water quality. 55% of measurements were deeper than 0.9 m.

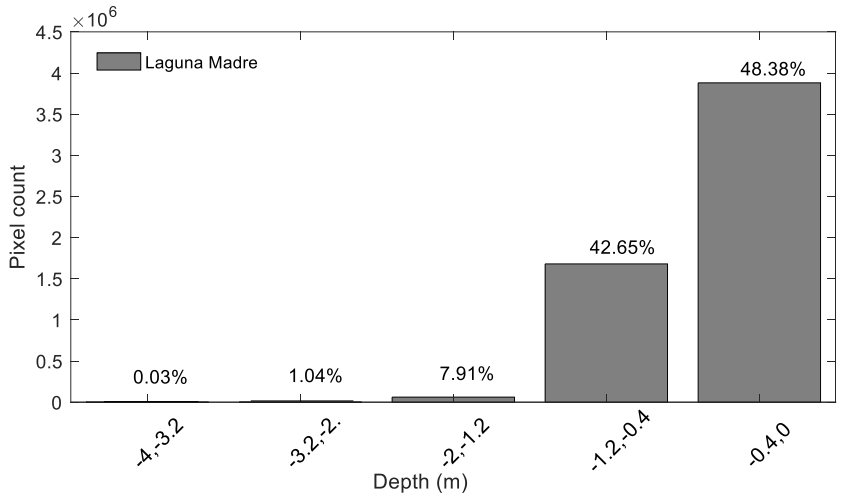

Figure 26-d: ALB analysis of entire lagoon. Mean depth was 0.61 m. 42.65% of all depths were in between 0.4 and 1.2 m.

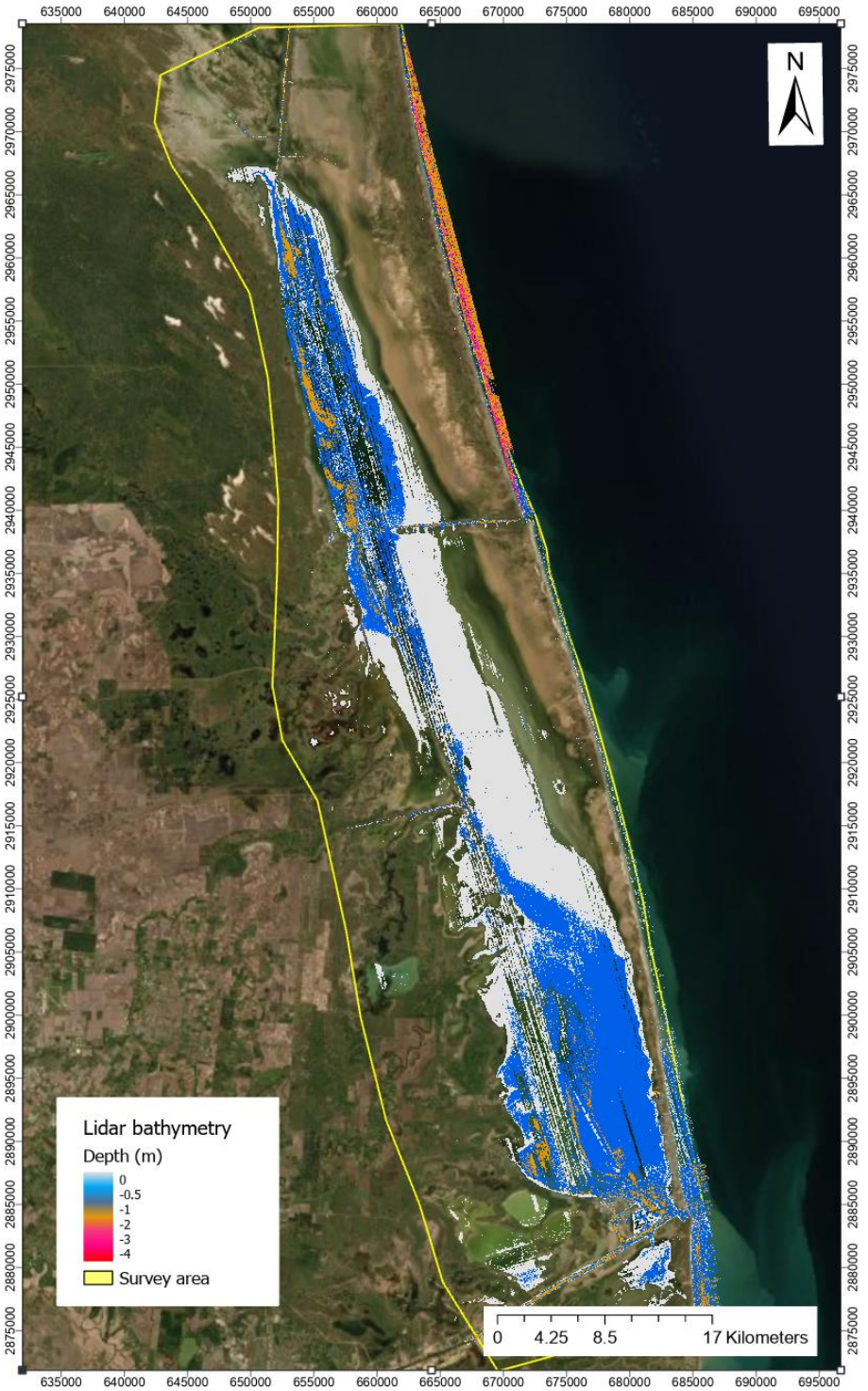

Figure 27: Lidar bathymetry of Lower Laguna Madre. Particularly in the transparent areas of the lagoon and in the northern Gulf coast shoreline, Lidar measured the bottom with high detail, where 51% of the bottom were measured deeper than 0.4 m.

g) Satellite derived bathymetry (SDB)

BEG investigated satellite derived bathymetry in Laguna Madre using multi-band imagery of multiple years. Depth maps were generated using ENVI v5.5's SPEAR algorithm where different *in-situ* measurements were input for each year. Results revealed discrepancy with depth ranges (1.58 to 2.54 m), and standard deviation varied moderately (0.35-0.46 m, Table 16). For the analysis, SDB results of 2017 imagery was used as the *principal* QC metric (benchmark) and results were compared to airborne Lidar bathymetry, where data acquisition dates of both platforms overlapped (Table 17). However, for study purposes, in Area #1, the depth difference was investigated of all imagery (2016-2019). Because of 20-m coarse grid spacing of SDB, the default QC algorithm threshold distance was extended (2-5 m) to include more measurements in the computations. Additionally, the tidal influence was considered with each satellite imagery corresponding to sensing time and depths were adjusted.

Findings revealed varying depth differences for each year. For instance, in 2017, SDB indicated deeper (mean = 7 cm), and conversely, in 2016, Lidar measured deeper (mean=21 cm). Because of the fundamental differences in the measuring technologies (e.g., active versus passive remote sensing, platform height, grid sampling); this amount of variation was expected. However, high RMSE values (21-35 cm) indicated correlation issues between the measurements. The shallow depths, varying surface and bottom properties and water quality were the major sources of bathymetric difference between the technologies (Table 18).

To understand the correlation in quantitative terms, the probability distribution of the results was investigated using the cumulative distribution function (CDF). A *cumulative probability* refers to the probability that the value of a random variable falls within a specified range, and indicates if the distribution is normal (Gabbiani and Cox, 2010). Results revealed that Lidar returns formed *normal distribution* with greater variance, where satellite measurements followed a *skewed distribution* and typically had smaller variance (**Figures 28-31**). For study purposes, profile of depths was plotted in Area #2 (2017) where Lidar returns were paired to satellite measurements using the QC algorithm. Because of higher concentration of turbidity, Lidar returns were scattered (measurement range=2.11 m) and produced greater standard deviation (19 cm), where SDB followed largely a linear depth representation (measurement range=0.24 m) with less significant standard deviation (SD=6 cm, **Figure 32**).

Additionally, DEM maps were constructed, and they were compared to SDB of entire lagoon (20 m grid size, 2017) to Lidar bathymetry of the lagoon. Mean depth difference was 0.69 m, and standard deviation produced an acceptable 0.46 m (**Figure 33**). Especially in the south-eastern and north-western

parts, the SDB and ALB matched to each other, increasing confidence in the complementary use technologies where water quality was higher.

Table 16: SDB analysis as generated by ENVI's SPEAR algorithm. The depth range was the lowest in 2017 due to tight thresholding with additional sonar measurements. The mean depth difference was less than 5 cm for all years, which is an indicative of reliability with the SDB analysis.

Imagery	Minimum depth (m)	Maximum depth (m)	Depth range (m)	Mean depth (m)	Standard deviation (m)
2016	0	-2.34	2.34	0.15	0.35
2017	0.52	-1.58	2.10	0.15	0.39
2018	0.53	-1.71	2.24	0.18	0.44
2019	0	-2.54	2.54	0.20	0.46

Table 17: Comparison of SDB analysis to ALB, in 2017. Area #3 was covered with clouds (N/A).

Location	Algorithm triangle (m)/ dZ tolerance (m)/ slope (degree)	Algorithm match (%)	Mean ALB (m)	Mean SDB (m)	Mean difference (m)	RMSE (m)
Area 1	5/1/45	59	0.83	0.89	-0.06	0.21
Area 2	5/1/45	45	1.18	0.93	0.25	0.31
Area 3	N/A					

Table 18: SDB accuracy comparison to Lidar bathymetry in survey Area#1. Overall depth discrepancy was low; however, high RMSE values indicated weak correlation. Survey area was shallow (< 1 m) and had relatively good water quality (mean turbidity=2.7 NTU).

Imagery	Algorithm triangle (m)/ dZ tolerance (m)/ slope (degree)	Algorithm match (%)	Mean ALB (m)	Mean SDB (m)	Mean difference (m)	RMSE (m)
2016	2/1/45	31	0.82	0.60	0.21	0.35
2016	5/1/45	64	0.83	0.61	0.21	0.33
2017	2/1/45	28	0.82	0.89	-0.07	0.22
2017	5/1/45	59	0.83	0.89	-0.06	0.21

2018	2/1/45	28	0.82	0.72	0.10	0.24
2018	5/1/45	58	0.83	0.72	0.11	0.24
2019	2/1/45	26	0.80	0.89	-0.09	0.25
2019	5/1/45	56	0.82	0.89	-0.07	0.23

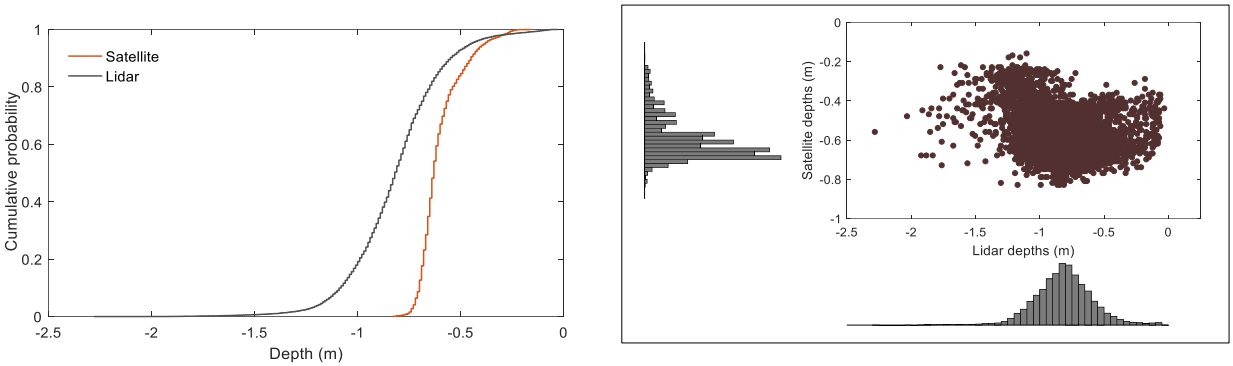

Figures 28 (a, b): Cumulative distribution of SDB versus ALB in 2016, in Area #1. Lidar measured deeper (mean difference=21 cm) and formed a normal distribution (SD= 0.22 m, σ^2=0.046 m) compared to SDB results (SD=0.1 m, σ^2=0.01 m).

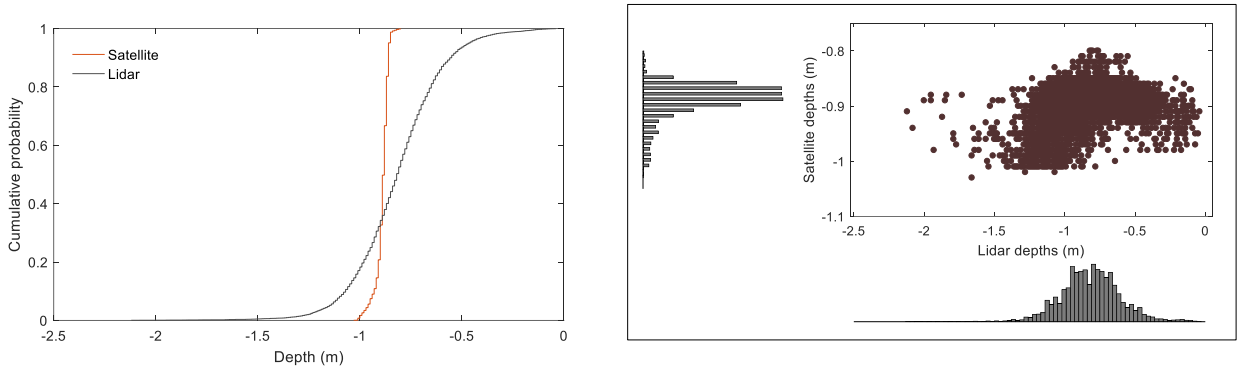

Figures 29 (a, b): SDB versus ALB in 2017, in Area #1. SDB measured deeper (mean difference=7 cm) and formed a skewed distribution (skewness = -1.45 m), where Lidar returns formed a normal distribution (skewness = -0.11 m). Figure 32 illustrates the linear form of SDB in this area.

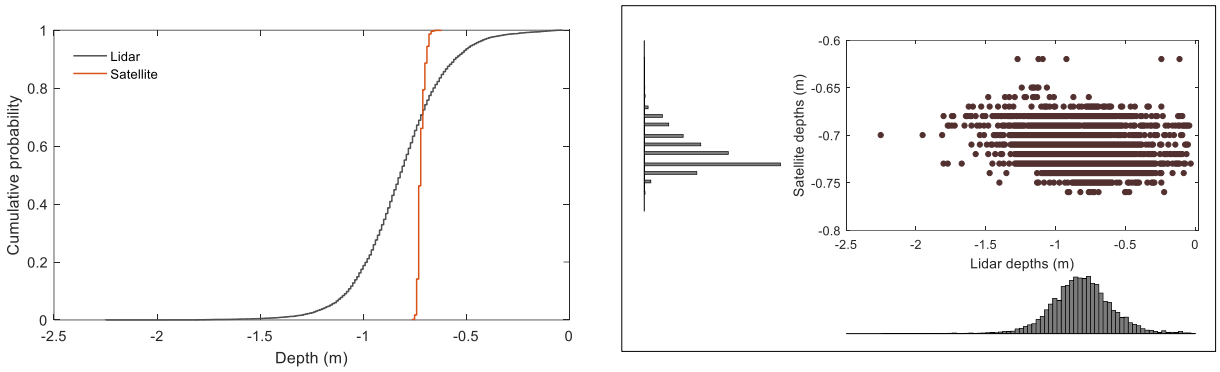

Figures 30 (a, b): SDB versus ALB in 2018, in Area #1. Lidar measured deeper (mean=0.1 m), and measurements were scattered (SD=0.21 m). SDB were almost uniform (measurement range =0.14 m) and produced a skewed depth distribution (0.92 m).

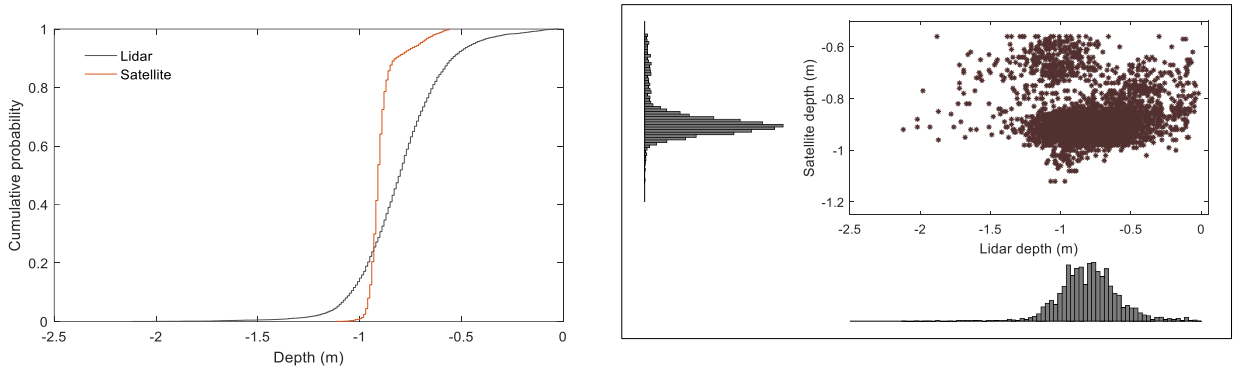

Figures 31 (a, b): SDB versus ALB in 2019, in Area #3. Overall, SDB produced deeper (mean discrepancy=0.09 m) and registered lower standard deviation (0.07 m). ALB formed a normal distribution with greater measurement range (2.1 m) compared to the SDB results (0.56 m).

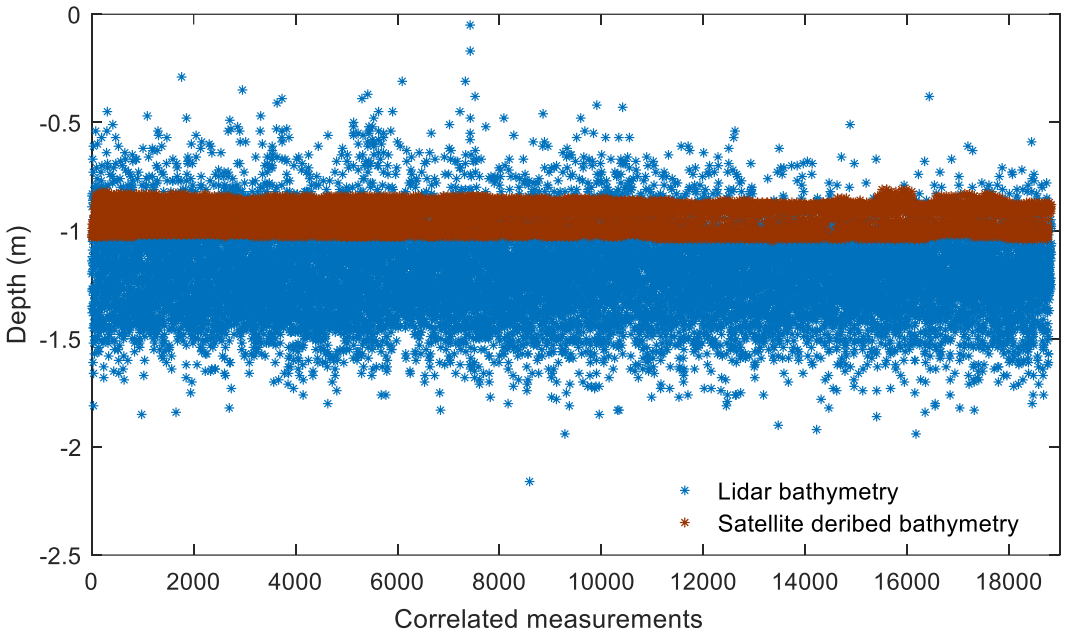

Figure 32: ALB (blue, mean depth=1.18 m) versus SDB (brown, mean depth=0.93 m) in Area #2 (2017). Notice the scattered form of Lidar returns in the water column compared to the mostly uniform and linear structure of SDB.

Figure 33: Map of ALB versus SDB in 2017. The mean depth difference=0.69 m, and standard deviation=0.46 m. In the southeastern and the northern sections of the lagoon, water quality was higher, and the disparity was marginal (green areas).

h) SDB-based spatio-temporal analysis

In this study, SDB findings of Laguna Madre were analysed over a period of four years. Spatio-temporal analysis is conducted by comparing the results of same metrics applied to different time periods, or temporal snapshots of the spatial data sets. For this purpose, SDB analysis of 2017 imagery was used as the benchmark and compared to the other SDB results produced by the SPEAR algorithm using Global Mapper v.20. Because of coarse grid sampling of Sentinel-2A NIR band, each pixel represented a 20 m surface. Table 19 presents the comparison findings, where the mean depth difference was less than 5 cm compared to 2017 depths. Because the difference was not substantial, it represented consistency with the morphologic variation of the lagoon over the years, and the robustness of SDB analysis with ENVI's SPEAR algorithm. **Figures 34-36** illustrate the distribution of pixel count differences of each year compared to 2017 depths. **Figures 37 a-d** present the analysis findings in map forms, where most differences appeared in lower water quality sections of the lagoon (southwest and central east).

Table 19: SDB spatio-temporal analysis of Laguna Madre over a period of four years. Of all years compared to 2017 depths, the mean difference was less than 5 cm.

Analysis	Minimum difference (m)	Maximum difference (m)	Mean difference (m)	Standard deviation (m)
2016-2017	-2.34	1.42	-0.02	0.31
2018-2017	-1.73	1.93	-0.03	0.29
2019-2017	-2.73	1.42	-0.05	0.30

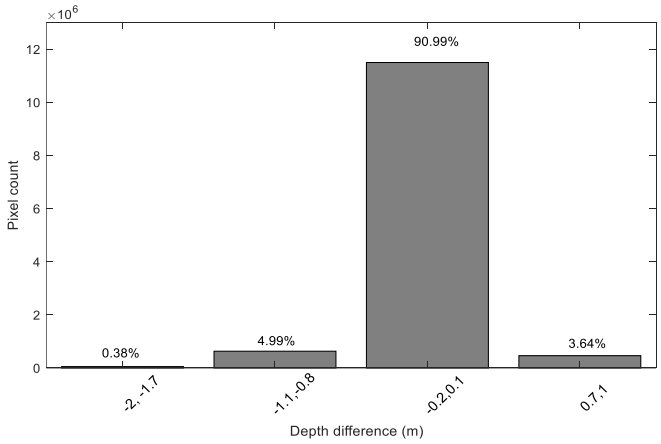

Figure 34: 2016 to 2017, SDB differences (2016 minus 2017 depths) as calculated from Global Mapper v.20. Computations indicated the mean depth difference at 2 cm and standard deviation was 0.32 m. 91% of the differences occurred between -0.2 and 0.1 m depths.

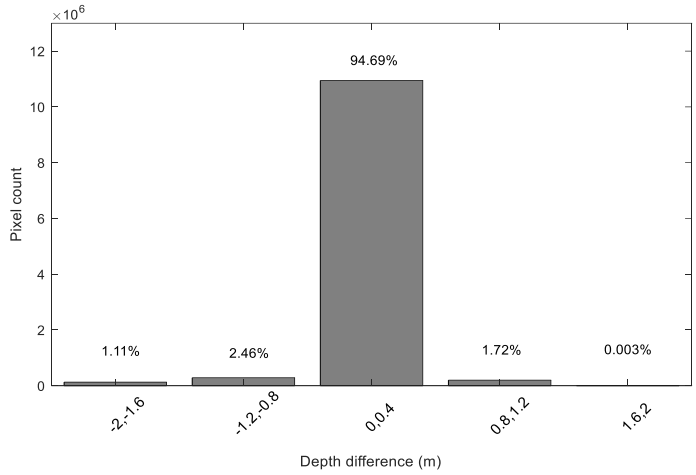

Figure 35: 2018 to 2017, SDB differences (2018 minus 2017 depths) as calculated from Global Mapper v.20. In the transparent sections of the lagoon, the depth difference was minimal; the mean depth difference was 3 cm and standard deviation was 0.3 m. 94% of depth differences was less than 0.4 m.

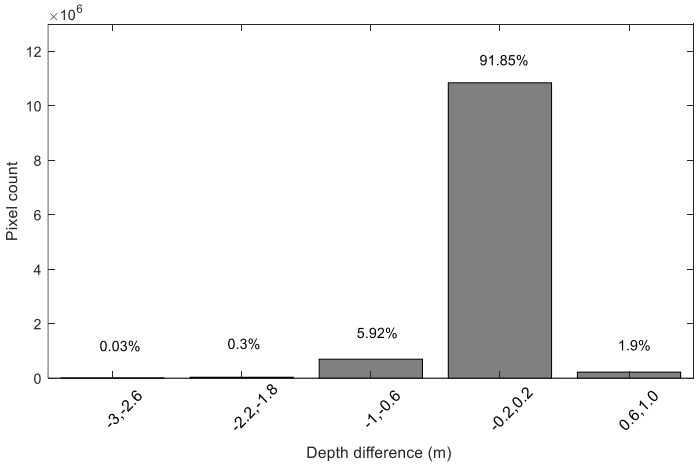

Figure 36: 2019 to 2017 satellite bathymetry differences (2019 minus 2017 depths) as calculated using Global Mapper v.20. Results revealed significant variations in the deeper sections of the lagoon (~ 6%, > 0.6 m).


(A) 2017
N
SDB - 2017
Depth (m)
> 1.4
1
0.7
0.4
0.1
< -0.2
Survey area
0 4.25 8.5 17 Kilometers


(B) 2016-2017
N
Difference (2016 versus 2017)
Depth (m)
1
0
-0.5
-1
-2
Survey area
0 4.25 8.5 17 Kilometers


(C) 2018-2017
N
Difference (2018 versus 2017)
Depth (m)
2
1
0
-1
-2
Survey area
0 4.25 8.5 17 Kilometers


(D) 2019-2017
N
Difference (2019 versus 2017)
Depth (m)
1
0
-1
-2
-3
Survey area
0 4.25 8.5 17 Kilometers

Figures 37 a-d: Figures present the SDB analysis of Laguna Madre using ENVI's SPEAR algorithm. Each year was compared to 2017 depths (Fig. 38-a). In 2016, comparison results revealed that 2017 SDB measured slightly deeper, where substantial change occurred in the northern section of the lagoon (marked with red). SDB did not produce significant depth differences in the central and southwest sections (Fig. 38-b). In 2018, the depth difference was minimal, where 94% of the differences were less than 4 cm (Fig. 39- c). In 2019, the lagoon sections with higher water quality (northeast and southwest) produced greater differences, where 6% of differences were deeper than 0.6 m (Fig. 38-d).

i) Lidar topography

BEG researchers output the entire NIR Lidar returns of hard and water surfaces in the survey area. NIR returns of water surfaces were filtered by examining and classifying the return amplitudes. However, because the lagoon was large and had fluctuating water quality, NIR return amplitudes from water surfaces varied greatly, causing irregularities with data output and respective classification. Particularly, excessive turbidity and very shallow depths increased the typical backscatter amplitude (water degrades the amplitude rapidly) and the amount of reflection from such surfaces. Therefore, with each vector data tile, manual editing was completed using Microstation v8i TerraScan application that were not classified correctly by the algorithm. **Figure 38** presents the topographic surface heights in Laguna Madre, where more than half of the elevations (52.6%) registered between 0.94-2.4 m, therefore, we computed a mean elevation of 2.35 m. Only 0.3% of all heights measured were greater than 11.2 m. The NIR data analysis revealed hard surfaces below the mean sea level, particularly in the northeastern section where mud holes were evident; therefore, the minimum height threshold was set to -2 m.

To build DEMs of vector data sets, LASTools utility "lasgrid.exe" application was used with the "fill" parameter set to 2 and 3 meters (i.e., fill 2). This option enabled the filling of void areas within a square radius by interpolation and averaging of heights in the output raster file. However, because irregularities were evident in the data (e.g., **Figure 39**), BEG processed and included NIR DEMs of constructed by certain "fill" parameters. In the data delivery, unobstructed and unedited NIR data sets were included that may be beneficial to certain data analysts. **Figure 40** presents the topographic map of hard surfaces surrounding the lagoon.

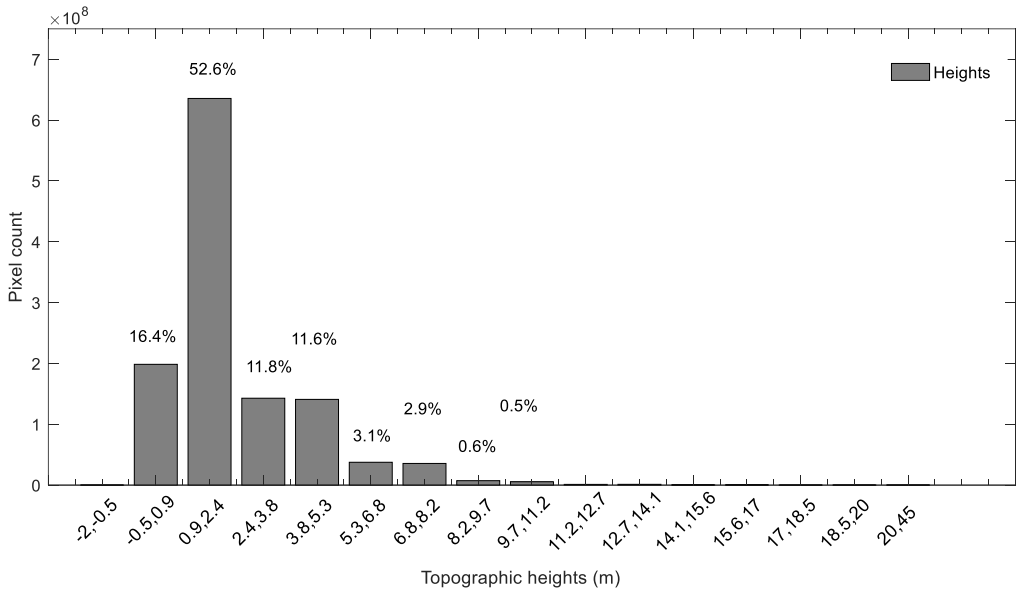

Figure 38: Topographic heights in Laguna Madre. Heights range from -2 m to 45 m.

Figure 39: Visible NIR Lidar irregularities caused by the classification algorithm. Height interpolation and averaging method with neighbouring distance parameters were used to fill some of these void areas.

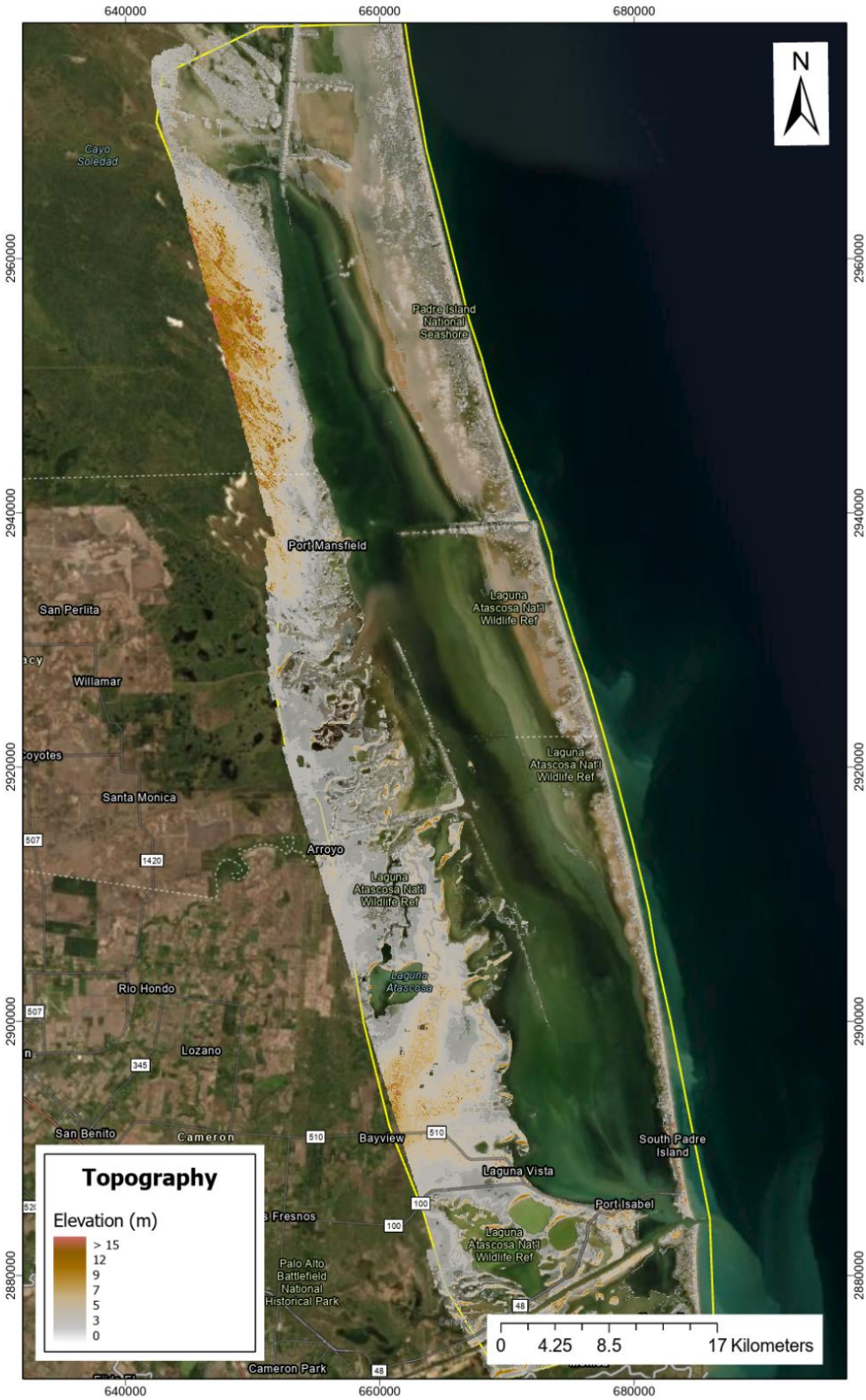

Figure 40: Topography of hard surfaces surrounding Laguna Madre. The mean elevation is 2.35 m with highest peaks reaching 45 m above the water surface.

5) Conclusions

In this study, BEG processed and analyzed previously acquired ALB data sets of Laguna Madre, and quantified the topographic heights and depth accuracies using other available survey technologies. The reflectance analysis was conducted to understand the surface properties and to classify the lagoon with regards to varying water quality. Results assisted to build masks to identify transparent sections of the lagoon, and to conduct further bathymetric analysis as applicable. ALB and SDB assessments identified the depth characteristics of the lagoon, and analysis of multiple years helped explore the temporal changes occurred in the lagoon. Further, depths were assessed whether the findings met or exceeded the established international hydrographic standards.

The study demonstrated that in such survey locations, depth measurements using remote sensing technology were influenced with environmental conditions and add complexity to building wholesome bathymetric maps. Overall, study revealed the following statements:

- Application of quality control methods is fundamental to understand the height and depth accuracies produced by ALB prior to building DEMs or merging data sets acquired by different platforms.
- Mapping with ALB has practical and theoretical limitations in large and dynamic shallow waters. The technology is effective and very detailed to measure depths; however, environmental conditions influence the results and the wholeness of the data sets.
- Utilizing satellite imagery can be cost-effective and complementary method for shallow water mapping; however, the results can be skewed with varying depth and environmental conditions.
- ALB is vastly detailed compared to satellite derived bathymetry. Coarse grid sampling of satellite bathymetry prevents comprehensive depth comparison between the technologies; however, results in this study indicated acceptable depth measurements particularly in transparent sections of the lagoon.

BEG recommends that future work in Laguna Madre should include the merging of ALB and multi-beam sonar data sets to build a comprehensive and a whole bathymetric map. Because sensing platforms and structure of data sets are fundamentally different, application of quality control methods is critical.

Acknowledgement

This project was supported by contract no. TWDB NO. 2101792506 between Texas Water Development Board and the Bureau of Economic Geology, The University of Texas at Austin. Kutalmis Saylam served as the principal investigator and Alejandra Briseno analysed satellite imagery. TWDB Coastal Flood Modeler Amin Kiaghadi served as project manager. Joey Thomas of TWDB supplied critical feedback and project support. Caimee Schoenbaechler, Manager of Coastal Sciences program TWDB, inquired about the project and has overseen the budgeting aspects. Aspen Helicopters of California provided survey aircraft and pilots for the airborne lidar survey. BEG staff Jeff Paine served as contract PI to secure funding from Texas General Land Office for data acquisition. BEG researcher Aaron Averett operated airborne lidar instrument and BEG researchers John Hupp and John Andrews participated in field work and data processing. We thank all those others who were involved and made this comprehensive study possible. With our efforts, we sincerely hope to contribute to the hydrographic mapping community utilizing remote sensing technologies.

References

Aguilar, F.J., Mills, Jon.P., 2008. Accuracy assessment of lidar-derived digital elevation models. The Photogrammetric Record 23, 148–169. https://doi.org/10.1111/j.1477-9730.2008.00476.x

Ahmad, A., Sufahani, S.F., 2012. Analysis of Landsat 5 TM data of Malaysian land covers using ISODATA clustering technique, in: 2012 IEEE Asia-Pacific Conference on Applied Electromagnetics (APACE). Presented at the 2012 IEEE Asia-Pacific Conference on Applied Electromagnetics (APACE), IEEE, Melaka, Malaysia, pp. 92–97. https://doi.org/10.1109/APACE.2012.6457639

Ashphaq, M., Srivastava, P.K., Mitra, D., 2021. Review of near-shore satellite derived bathymetry: Classification and account of five decades of coastal bathymetry research. Journal of Ocean Engineering and Science 6, 340–359. https://doi.org/10.1016/j.joes.2021.02.006

ASPRS, 2015. ASPRS Positional Accuracy Standards for Digital Geospatial Data. photogramm eng remote sensing 81, 1–26. https://doi.org/10.14358/PERS.81.3.A1-A26

B Delaunay, 1932. Sur la sphere vide - A la memoire de Georges Voronoi.

Beć, K.B., Huck, C.W., 2019. Breakthrough Potential in Near-Infrared Spectroscopy: Spectra Simulation. A Review of Recent Developments. Front. Chem. 7, 48. https://doi.org/10.3389/fchem.2019.00048

Bramich, J., Bolch, C.J.S., Fischer, A., 2021. Improved red-edge chlorophyll-a detection for Sentinel 2. Ecological Indicators 120, 106876. https://doi.org/10.1016/j.ecolind.2020.106876

Brock, J.C., Purkis, S.J., 2009. The emerging role of Lidar remote sensing in coastal research and resource management. Journal of Coastal Research 10053, 1–5. https://doi.org/10.2112/SI53-001.1

Caudle, T.L., Paine, J.G., Andrews, J.R., Saylam, K., 2019. Beach, Dune, and Nearshore Analysis of Southern Texas Gulf Coast Using Chiroptera LIDAR and Imaging System. Journal of Coastal Research 35, 251. https://doi.org/10.2112/JCOASTRES-D-18-00069.1

Csanyi, N., Toth, C.K., 2007. Improvement of Lidar Data Accuracy Using Lidar-Specific Ground Targets. Photogrammetric Engineering & Remote Sensing 73, 385–396. https://doi.org/10.14358/PERS.73.4.385

Darama, Y., Selek, Z., Selek, B., Akgul, M.A., Dagdeviren, M., 2019. Determination of sediment deposition of Hasanlar Dam using bathymetric and remote sensing studies. Nat Hazards 97, 211–227. https://doi.org/10.1007/s11069-019-03635-y

Delegido, J., Verrelst, J., Alonso, L., Moreno, J., 2011. Evaluation of Sentinel-2 Red-Edge Bands for Empirical Estimation of Green LAI and Chlorophyll Content. Sensors 11, 7063–7081. https://doi.org/10.3390/s110707063

Favoretto, F., Morel, Y., Waddington, A., Lopez-Calderon, J., Cadena-Roa, M., Blanco-Jarvio, A., 2017. Testing of the 4SM Method in the Gulf of California Suggests Field Data Are not Needed to Derive Satellite Bathymetry. Sensors 17, 2248. https://doi.org/10.3390/s17102248

Fernandez-Diaz, J., Carter, W., Shrestha, R., Glennie, C., 2014. Now You See It… Now You Don't: Understanding Airborne Mapping LiDAR Collection and Data Product Generation for Archaeological Research in Mesoamerica. Remote Sensing 6, 9951–10001. https://doi.org/10.3390/rs6109951

Flood, M., 2004. ASPRS guidelines. Vertical accuracy reporting for lidar data. (Guidelines). American Society of Photogrammetry and Remote Sensing.

Gabbiani, F., Cox, S.J., 2010. Probability and Random Variables, in: Mathematics for Neuroscientists. Elsevier, pp. 155–173. https://doi.org/10.1016/B978-0-12-374882-9.00011-3

Gao, B., 1996. NDWI—A normalized difference water index for remote sensing of vegetation liquid water from space. Remote Sensing of Environment 58, 257–266. https://doi.org/10.1016/S0034-4257(96)00067-3
Gernez, P., Lafon, V., Lerouxel, A., Curti, C., Lubac, B., Cerisier, S., Barillé, L., 2015. Toward Sentinel-2 High Resolution Remote Sensing of Suspended Particulate Matter in Very Turbid Waters: SPOT4 (Take5) Experiment in the Loire and Gironde Estuaries. Remote Sensing 7, 9507–9528. https://doi.org/10.3390/rs70809507
Guenther, G.C., Cunningham, A.G., LaRocque, P.E., Reid, D.J., 2000. Meeting the accuracy challenge in airborne bathymetry (No. ADA488934). National Oceanic Atmospheric Administration/Nesdis Silver Spring MD.
Habib, A., Bang, K.I., Kersting, A.P., Lee, D.-C., 2009. Error Budget of Lidar Systems and Quality Control of the Derived Data. Photogrammetric Engineering & Remote Sensing 75, 1093–1108. https://doi.org/10.14358/PERS.75.9.1093
IHO, 2020. International Hydrographic Organization, Standards for Hydrographic Surveys (Special publication No. S-44 Edition 6.0.0). International Hydrographic Bureau, Monaco.
Jerlov, N.G., 1976. Chapter 3-Beam Attenuation, in: Elsevier Oceanography Series, Marine Optics. Elsevier, pp. 47–66. https://doi.org/10.1016/S0422-9894(08)70795-5
Johansen, R., Beck, R., Nowosad, J., Nietch, C., Xu, M., Shu, S., Yang, B., Liu, H., Emery, E., Reif, M., Harwood, J., Young, J., Macke, D., Martin, M., Stillings, G., Stumpf, R., Su, H., 2018. Evaluating the portability of satellite derived chlorophyll-a algorithms for temperate inland lakes using airborne hyperspectral imagery and dense surface observations. Harmful Algae 76, 35–46. https://doi.org/10.1016/j.hal.2018.05.001
Kaufmann, J.E., 2019. USGS Lidar Base Specification.
Khorram, S. (Ed.), 2012. Remote sensing, SpringerBriefs in space development. Springer, Berkeley, CA.
Klemas, V., 2011. Beach profiling and Lidar Bathymetry: An overview with case studies. Journal of Coastal Research 277, 1019–1028. https://doi.org/10.2112/JCOASTRES-D-11-00017.1
Mandlburger, G., Pfennigbauer, M., Pfeifer, N., 2013. Analyzing near water surface penetration in laser bathymetry - A case study at the River Pielach. ISPRS Annals of Photogrammetry, Remote Sensing and Spatial Information Sciences II-5/W2, 175–180. https://doi.org/10.5194/isprsannals-II-5-W2-175-2013
McManus, J., 1990. Hydrodynamics of estuaries edited by Bjorn Kjerfve, vol II estuarine case studies, CRC press, 1988. No. of pages: 125. Earth Surf. Process. Landforms 15, 384–385. https://doi.org/10.1002/esp.3290150411
Mondejar, J.P., Tongco, A.F., 2019. Estimating topsoil texture fractions by digital soil mapping - a response to the long outdated soil map in the Philippines. Sustain Environ Res 29, 31. https://doi.org/10.1186/s42834-019-0032-5
Monteys, X., Harris, P., Caloca, S., Cahalane, C., 2015. Spatial Prediction of Coastal Bathymetry Based on Multispectral Satellite Imagery and Multibeam Data. Remote Sensing 7, 13782–13806. https://doi.org/10.3390/rs71013782
Muller, J.M., 2017. Indirect soil salinity detection in irrigated areas using earth observation methods (Master's thesis). Stellenbosch University, Netherlands.
Najar, M.A., Benshila, R., Bennioui, Y.E., Thoumyre, G., Almar, R., Bergsma, E.W.J., Delvit, J.-M., Wilson, D.G., 2022. Coastal Bathymetry Estimation from Sentinel-2 Satellite Imagery: Comparing Deep Learning and Physics-Based Approaches. Remote Sensing 14, 1196. https://doi.org/10.3390/rs14051196
Paine, J.G., Andrews, J.R., Saylam, K., Tremblay, T.A., 2015. Airborne Lidar-based Wetland and Permafrost-feature Mapping on an Arctic Coastal Plain, North Slope, Alaska: Wetlands Mapping,

Lake Volumes, and Permafrost Features, in: Remote Sensing of Wetlands: Applications and Advances. CRC Press, Boca Raton, FL, pp. 413–434.
Paine, J.G., Caudle, T., Andrews, J.R., 2013. Shoreline, beach, and dune morphodynamics, Texas Gulf Coast (Technical contract report). Bureau of Economic Geology, The University of Texas at Austin, Austin, Texas.
Paine, J.G., Caudle, T.L., Andrews, J.R., 2017. Shoreline and Sand Storage Dynamics from Annual Airborne LIDAR Surveys, Texas Gulf Coast. Journal of Coastal Research 333, 487–506. https://doi.org/10.2112/JCOASTRES-D-15-00241.1
Petrie, G., Toth, C.K., 2018. Introduction to Laser ranging, profiling, and scanning, in: Topographic Laser Ranging and Scanning: Principles and Processing. Taylor & Francis, CRC Press, Boca Raton.
Quan, X., Fry, E.S., 1995. Empirical equation for the index of refraction of sea water. Applied Optics 34, 3477. https://doi.org/10.1364/AO.34.003477
Savitzky, Abraham., Golay, M.J.E., 1964. Smoothing and differentiation of data by simplified least squares procedures. Analytical Chemistry 36, 1627–1639. https://doi.org/10.1021/ac60214a047
Saylam, K., Brown, R.A., Hupp, J.R., 2017a. Assessment of depth and turbidity with airborne Lidar bathymetry and multiband satellite imagery in shallow water bodies of the Alaskan North Slope. International Journal of Applied Earth Observation and Geoinformation 58, 191–200. https://doi.org/10.1016/j.jag.2017.02.012
Saylam, K., Hupp, J., Andrews, J., Averett, A., Knudby, A., 2018a. Quantifying Airborne Lidar Bathymetry Quality-Control Measures: A Case Study in Frio River, Texas. Sensors 18, 4153. https://doi.org/10.3390/s18124153
Saylam, K., Hupp, J.R., Aaron, R.A., 2017b. Quantifying the bathymetry of the lower Colorado River basin, Arizona, with airborne Lidar. Presented at the IGTF ASPRS 2017 Annual Conference, researchgate, Baltimore, Maryland, pp. 1–11.
Saylam, K., Hupp, J.R., Averett, A.R., Gutelius, W.F., Gelhar, B.W., 2018b. Airborne lidar bathymetry: assessing quality assurance and quality control methods with Leica Chiroptera examples. International Journal of Remote Sensing 39, 2518–2542. https://doi.org/10.1080/01431161.2018.1430916
Saylam, K., R. Averett, A., Costard, L., D. Wolaver, B., Robertson, S., 2020. Multi-Sensor Approach to Improve Bathymetric Lidar Mapping of Semi-Arid Groundwater-Dependent Streams: Devils River, Texas. Remote Sensing 12, 2491. https://doi.org/10.3390/rs12152491
Sebastiá-Frasquet, M.-T., Aguilar-Maldonado, J.A., Santamaría-Del-Ángel, E., Estornell, J., 2019. Sentinel 2 Analysis of Turbidity Patterns in a Coastal Lagoon. Remote Sensing 11, 2926. https://doi.org/10.3390/rs11242926
Shaffer, J.P., 1991. The Gauss—Markov Theorem and Random Regressors. The American Statistician 45, 269–273. https://doi.org/10.1080/00031305.1991.10475819
Shin, M.S., Yang, I.T., Lee, D.H., 2016. A Study on Airborne LiDAR Calibration and Operation Techniques for Bathymetric Survey. Journal of Korean Society for Geospatial Information System 24, 113–120. https://doi.org/10.7319/kogsis.2016.24.2.113
Stumpf, R.P., Holderied, K., Sinclair, M., 2003. Determination of water depth with high-resolution satellite imagery over variable bottom types. Limnology and Oceanography 48, 547–556. https://doi.org/10.4319/lo.2003.48.1_part_2.0547
Thenkabail, P., 2018. Remote Sensing Handbook - Three Volume Set, 1st ed. CRC Press. https://doi.org/10.1201/b19355
Vosselman, G., 2012. Automated planimetric quality control in high accuracy airborne laser scanning surveys. ISPRS Journal of Photogrammetry and Remote Sensing 74, 90–100. https://doi.org/10.1016/j.isprsjprs.2012.09.002

Wang, X., Ling, F., Yao, H., Liu, Y., Xu, S., 2019. Unsupervised Sub-Pixel Water Body Mapping with Sentinel-3 OLCI Image. Remote Sensing 11, 327. https://doi.org/10.3390/rs11030327

Zhu, Q., Zhang, Y., Li, F., 2008. Three-dimensional TIN algorithm for digital terrain modeling. Geo-spatial Information Science 11, 79–85. https://doi.org/10.1007/s11806-008-0043-6

Appendix A - Data acquisition mission log

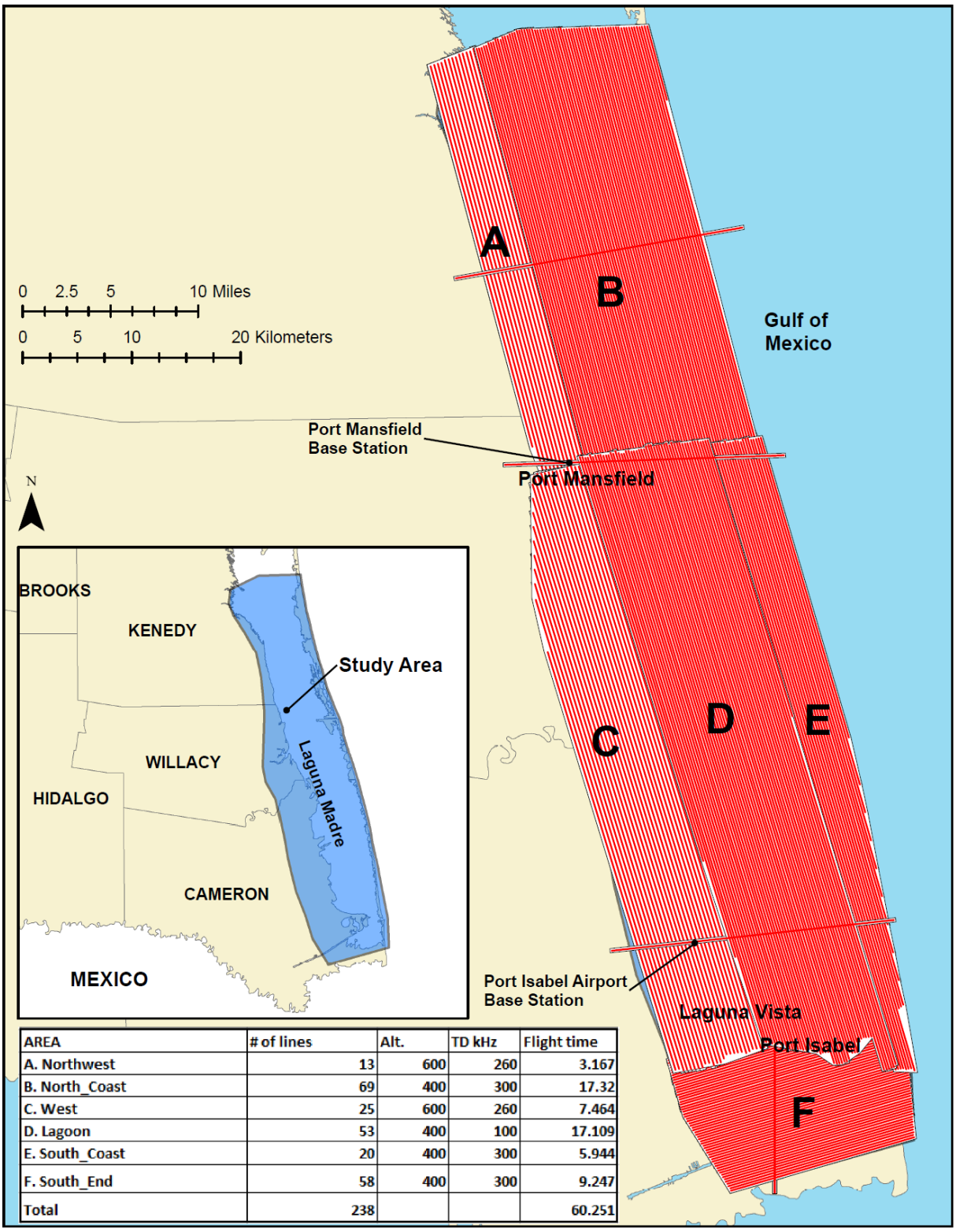

AREA	# of lines	Alt.	TD kHz	Flight time
A. Northwest	13	600	260	3.167
B. North_Coast	69	400	300	17.32
C. West	25	600	260	7.464
D. Lagoon	53	400	100	17.109
E. South_Coast	20	400	300	5.944
F. South_End	58	400	300	9.247
Total	238			60.251

Figure A-1: Sections A-F, illustrating the individual survey sections and duration of airborne campaigns in Laguna Madre. The survey area was fragmented into six sections for easier flight planning and data management purposes.

Date	Mission	Aircraft	Aircraft Operator	System Operator	Pilots	HOBSS meter ON	HOBSS meter OFF	Total duration (h: mm)	Airport	Survey block	Altitude (m AGL)	1064 nm PRF	515 nm PRF	Info
2017-04-28	A	N88N	Aspen	AA	Matt, MB	11:44	13:48	2:04	Pt. Isabel	A	Varies	200	35	Calibration
2017-04-30	A	N88N	Aspen	AA	Matt, MB	8:34	11:39	3:05	Pt. Isabel	A, B	600	200	35	Survey
2017-04-30	B	N88N	Aspen	AA	Matt, MB	13:10	15:31	2:21	Pt. Isabel	A, B	600	200	35	Survey
2017-04-30	C	N88N	Aspen	AA	Matt, MB	15:54	18:50	2:56	Pt. Isabel	C, D	600	200	35	Survey
2017-05-01	A	N88N	Aspen	AA	Matt, MB	9:23	13:08	3:45	Pt. Isabel	B, D	400	300, 100	35	Survey
2017-05-01	B	N88N	Aspen	AA	Matt, MB	14:20	17:45	3:25	Pt. Isabel	D	400	100	35	Survey
2017-05-02	A	N88N	Aspen	AA	Matt, MB	8:52	12:36	3:44	Pt. Isabel	E	400	30	35	Survey
2017-05-04	A	N88N	Aspen	AA	Matt, MB	8:30	11:08	2:38	Pt. Isabel	E	400	300	35	Survey
2017-05-04	B	N88N	Aspen	AA	Matt, Martin	12:21	15:39	3:18	Pt. Isabel	E, D, B, C	400, 600	270	35	Survey
2017-05-05	A	N88N	Aspen	AA	Matt, Rachel	8:58	12:06	3:08	Pt. Isabel	D	400	100	35	Survey
2017-05-05	B	N88N	Aspen	AA	Matt, Rachel	13:50	16:07	2:17	Pt. Isabel	D	400	100	35	Survey
2017-05-06	A	N88N	Aspen	AA	Matt, Rachel	8:38	11:17	2:39	Pt. Isabel	B, D	400	100, 300	35	Survey
2017-05-06	B	N88N	Aspen	AA	Matt, Rachel	12:55	14:20	1:25	Pt. Isabel	B, D	400	300, 100	35	Survey
2017-05-06	C	N88N	Aspen	AA	Matt, Rachel	5:10	8:30	3:20	Pt. Isabel	B, D	400	300, 100	35	Survey
2017-05-07	A	N88N	Aspen	AA	Matt, Rachel	9:52	13:12	3:20	Pt. Isabel	B, D	400	300	35	Survey
2017-05-07	B	N88N	Aspen	AA	Matt, Rachel	14:50	17:31	2:41	Pt. Isabel	B, D	400	300	35	Survey
2017-05-07	C	N88N	Aspen	AA	Matt, Rachel	18:17	21:06	2:49	Pt. Isabel	B, D	400	300	35	Survey
2017-05-08	A	N88N	Aspen	AA	Matt, Rachel	17:32	20:41	3:09	Pt. Isabel	B, D	400	300	35	Survey
2017-05-09	A	N88N	Aspen	AA	Matt, Rachel	11:36	15:05	3:29	Pt. Isabel	B, D	400	300	35	Survey
2017-05-09	B	N88N	Aspen	AA	Matt, Rachel	16:17	19:30	3:13	Pt. Isabel	B, D, F	400	300	35	Survey
2017-05-10	A	N88N	Aspen	AA	Matt, Rachel	9:58	13:30	3:32	Pt. Isabel	C, F	400, 600	200, 300	35	Survey
2017-05-10	B	N88N	Aspen	AA	Matt, Rachel	14:30	17:09	2:39	Pt. Isabel	A, B, C	400, 600	200, 300	35	Survey
2017-05-10	C	N88N	Aspen	AA	Matt, Rachel	17:45	19:22	1:37	Pt. Isabel	C	600	200	35	Survey
2017-05-11	A	N88N	Aspen	AA	Matt, Rachel	9:20	12:31	3:11	Pt. Isabel	F	400	300	35	Survey
2017-05-11	B	N88N	Aspen	AA	Matt, Rachel	13:30	16:30	3:00	Pt. Isabel	F, C	400, 600	300, 195	35	Survey
2017-05-12	A	N88N	Aspen	AA	Matt, Rachel	9:30	12:16	2:46	Pt. Isabel	N/A	N/A	N/A	N/A	System malfunction
2017-05-13	A	N88N	Aspen	AA	Matt, Rachel	12:15	15:29	3:14	Pt. Isabel	D	400	295	35	Survey
2017-05-13	B	N88N	Aspen	AA	Matt, Rachel	16:32	19:48	3:16	Pt. Isabel	C, D	600, 400	200, 300	35	Survey
2017-05-14		N88N	Aspen	AA	Matt, Rachel	8:45	11:33	2:48	Pt. Isabel	B, D	400	300	35	Survey

Abbreviations

Aircraft ID: N88N
ALB system operator: Aaron Averett (AA)
Airborne campaign base airport: Port Isabel, TX
HOBBS meter: Aircraft engine ON and OFF time.
Pulse repetition rate (PRF): Lidar system pulse repetition speed (kHz)

Appendix B - Turbidity and localized sonar measurements

Location	Date	UTM E	UTM N	Reading 1	Reading 2	Reading 3	AVG NTU	Secchi (m)	*Kd*	WP SNR depth (m)	Avg. SNR depth (m)	Lidar depth CL0-CL7 (m)	Lidar depth CL0-CL10 (m)
2	2017-05-01	681989.95	2891306.11	0.60	0.70	0.61	0.64	VB	N/A	1.49	1.13	1.06	N/A
3	2017-05-01	682546.59	2891234.73	2.21	2.49	2.81	2.50	VB	N/A	1.85	1.83	1.08	2.16
4	2017-05-01	681723.88	2891259.92	2.10	2.02	2.01	2.04	VB	N/A	1.26	1.29	1.34	1.53
5	2017-05-01	680939.15	2891230.51	2.38	2.99	2.79	2.72	VB	N/A	1.38	1.38	1.42	1.50
6	2017-05-01	681101.49	2890944.68	1.60	1.81	1.99	1.80	VB	N/A	1.35	1.38	1.40	1.47
7	2017-05-01	681434.53	2890731.42	1.90	2.16	2.24	2.10	VB	N/A	1.38	1.30	1.23	1.41
8	2017-05-01	681985.00	2890432.00	2.82	3.70	4.55	3.69	VB	N/A	1.33	1.33	1.37	1.47
9	2017-05-01	682282.75	2890039.69	2.81	3.18	3.26	3.08	VB	N/A	N/A	1.27	1.34	1.59
10	2017-05-01	681075.64	2889328.48	1.75	1.52	1.99	1.75	VB	N/A	1.19	1.22	1.11	1.40
11	2017-05-01	680624.58	2888914.09	3.36	3.62	4.10	3.69	VB	N/A	1.28	1.33	0.05	N/A
12	2017-05-01	680311.53	2889005.78	4.64	5.26	5.68	5.19	VB	N/A	1.45	1.44	1.44	1.63
13	2017-05-05	678831.78	2894403.48	1.31	1.51	1.59	1.47	VB	N/A	1.28	1.25	1.37	N/A
14	2017-05-05	678364.02	2894849.48	1.34	1.82	1.81	1.66	VB	N/A	1.19	1.21	1.35	1.38
15	2017-05-05	677943.08	2895043.14	2.79	2.93	3.39	3.04	VB	N/A	1.23	1.23	1.13	N/A
16	2017-05-05	677471.31	2895420.79	3.66	7.90	8.02	6.53	VB	N/A	1.40	1.40	1.49	1.63
17	2017-05-05	677293.56	2895990.83	3.78	11.50	12.20	9.16	VB	N/A	1.26	1.42	N/A	1.85
18	2017-05-05	676829.28	2896189.47	15.90	17.30	19.30	17.50	0.6	2.67	1.61	1.63	N/A	2.17
19	2017-05-05	677032.68	2897036.17	10.20	15.50	16.40	14.03	0.7	2.29	1.52	1.53	N/A	1.97
20	2017-05-05	677611.28	2897369.09	7.57	9.04	11.00	9.20	0.85	1.88	1.38	1.35	1.54	1.22
21	2017-05-05	677341.54	2898209.33	4.27	4.95	5.52	4.91	VB	N/A	1.45	1.41	1.67	1.72
22	2017-05-05	676915.17	2897588.56	8.69	11.50	12.30	10.83	0.7	2.29	1.57	1.54	1.27	1.59
23	2017-05-05	677020.09	2896493.08	10.50	12.80	12.70	12.00	0.9	1.78	1.57	1.57	N/A	2.58
24	2017-05-05	676501.32	2895309.69	14.00	18.90	19.70	17.53	0.8	2.00	1.66	1.67	N/A	N/A
25	2017-05-05	677336.30	2894813.24	3.85	3.43	3.90	3.73	VB	N/A	1.42	1.42	1.51	1.73
26	2017-05-12	672597.73	2888097.92	11.10	15.70	16.70	14.50	0.7	2.29	1.83	1.79	N/A	1.96
27	2017-05-12	673745.52	2887921.14	11.10	17.10	21.70	16.63	0.7	2.29	1.97	1.97	N/A	2.04
28	2017-05-12	674964.06	2887817.43	9.48	13.50	16.10	13.03	0.7	2.29	1.90	1.90	N/A	N/A
29	2017-05-12	676179.75	2887926.15	8.91	11.90	12.10	10.97	0.85	1.88	2.13	2.15	N/A	N/A
30	2017-05-12	676968.38	2888786.30	3.12	4.00	5.05	4.06	1.3	1.23	1.52	1.51	1.25	1.45
31	2017-05-12	675270.36	2888720.85	9.03	15.80	19.00	14.61	0.7	2.29	1.92	1.94	N/A	N/A
32	2017-05-12	674052.80	2888881.79	10.80	13.40	13.20	12.47	0.8	2.00	2.02	2.01	N/A	1.86
33	2017-05-12	674961.02	2889283.61	15.20	15.00	16.50	15.57	0.75	2.13	2.06	2.02	N/A	N/A
34	2017-05-12	676290.01	2889264.61	5.44	8.22	9.33	7.66	1	1.60	1.90	1.89	N/A	2.61
35	2017-05-12	676841.89	2889261.02	1.80	2.80	3.09	2.56	VB	N/A	1.59	1.55	1.33	1.51
36	2017-05-12	677419.18	2889228.25	2.47	3.33	4.08	3.29	VB	N/A	1.59	1.54	1.33	1.48

Abbreviations

UTM E: Universal Transverse Mercator – Easting (m)
UTM N: Universal Transverse Mercator – Northing (m)
Avg. NTU: Average measured turbidity in nephelometric turbidity unit
Secchi: Observed Secchi disk depth (m)
K_d: Diffuse attenuation coefficient
VB: Water bottom is visible to the observer
WP: Waypoint location marked for a sonar measurement
Avg. sonar depth: Average depth of all sonar measurements in 1-m radius
CL0: Class 0, surface, NIR + green wavelength, vector data
CL7: Class 7, bottom, green wavelength, standard bathymetric algorithm, vector data
CL10: Class 10, bottom, green wavelength, enhanced bathymetric algorithm, vector data

Appendix C - Reflectance

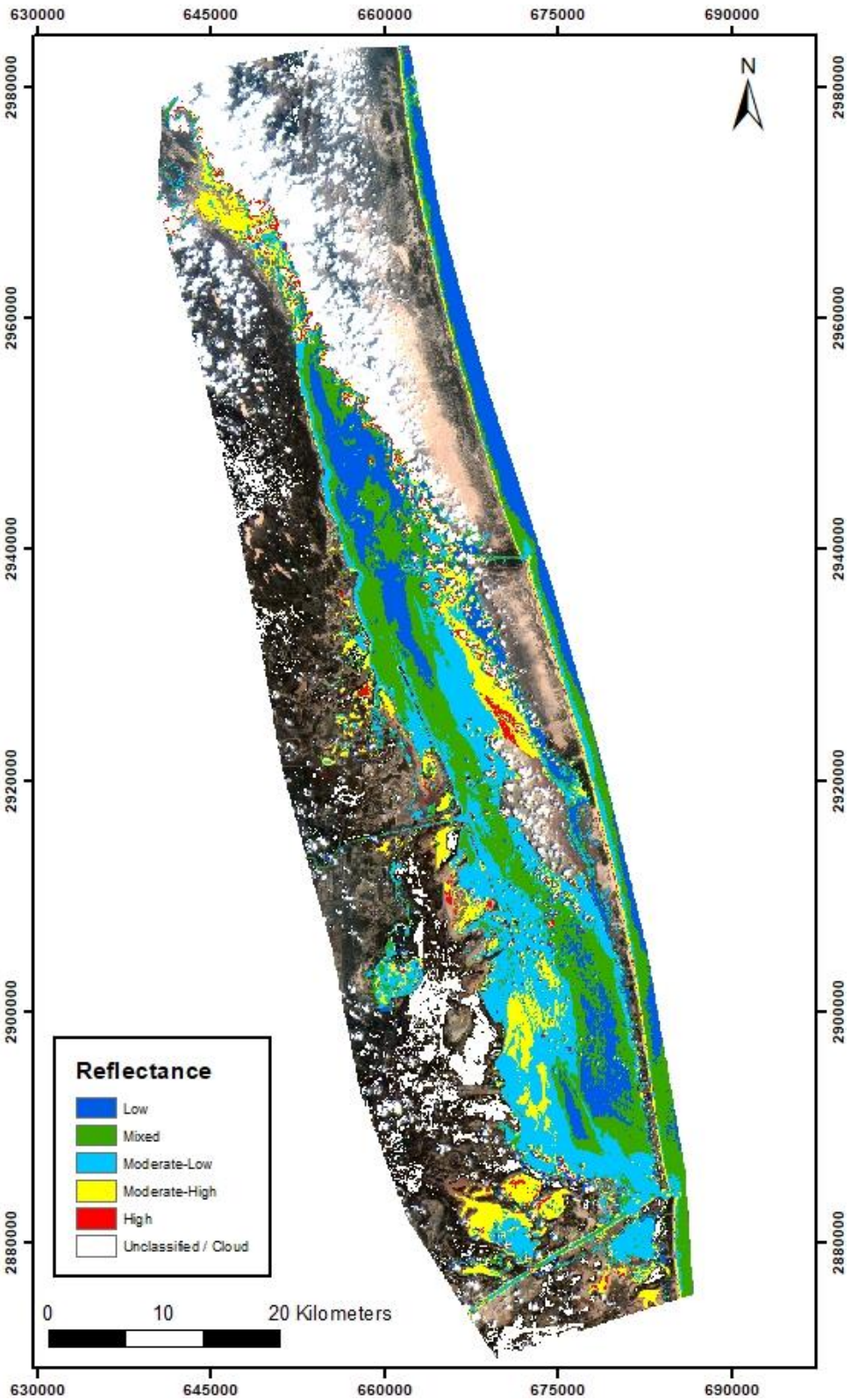

Figure C-1: Surface reflectance as recorded by 05/12/2016 Sentinel-2A L1C Band 5, classified using ENVI v5.5 Spectral Profile Tool. The northern and southern sections of the lagoon recorded lower reflectivity, corresponding to higher water quality.

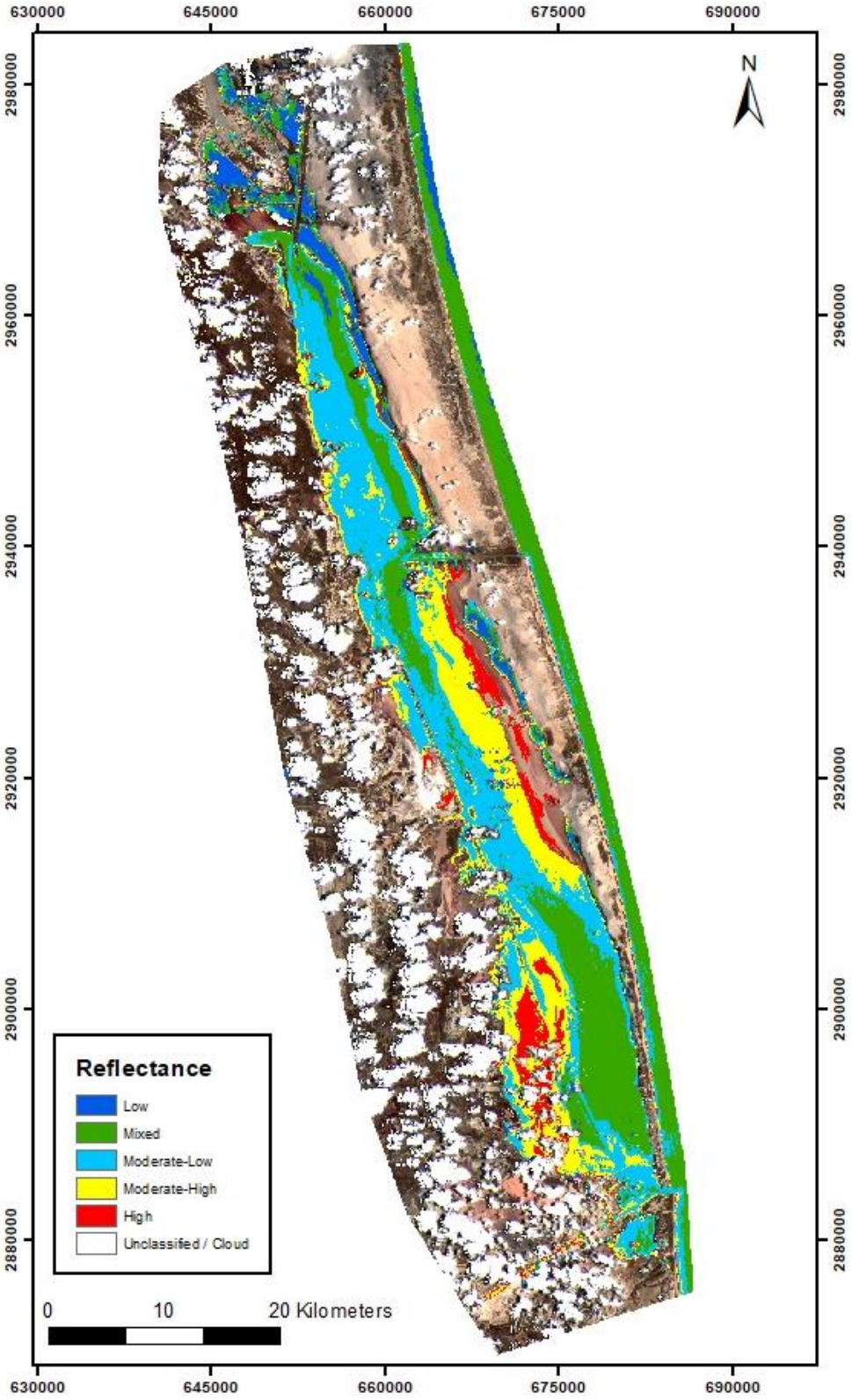

Figure C-2: Surface reflectance as recorded by 06/16/2017 Sentinel-2A L1C Band 5, classified using ENVI v5.5 Spectral Profile Tool. Water quality has decreased in the southwest and in the eastern parts of the lagoon, compared to the previous year.

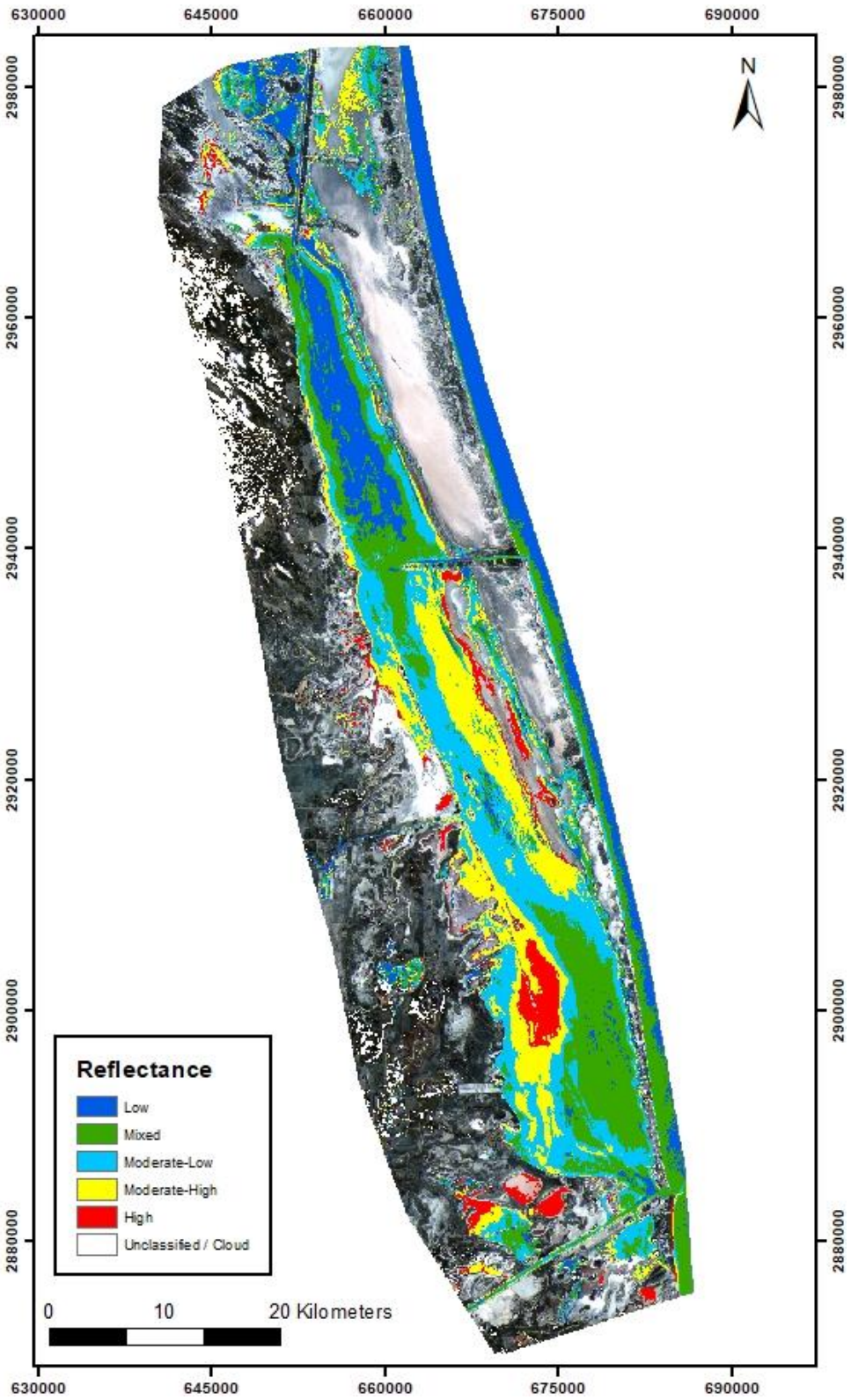

Figure C-3: Surface reflectance as recorded by 17/05/2018 Sentinel-2A L1C Band 5, classified using ENVI v5.5 Spectral Profile Tool. Water quality has increased substantially in the northern parts of the of the lagoon.

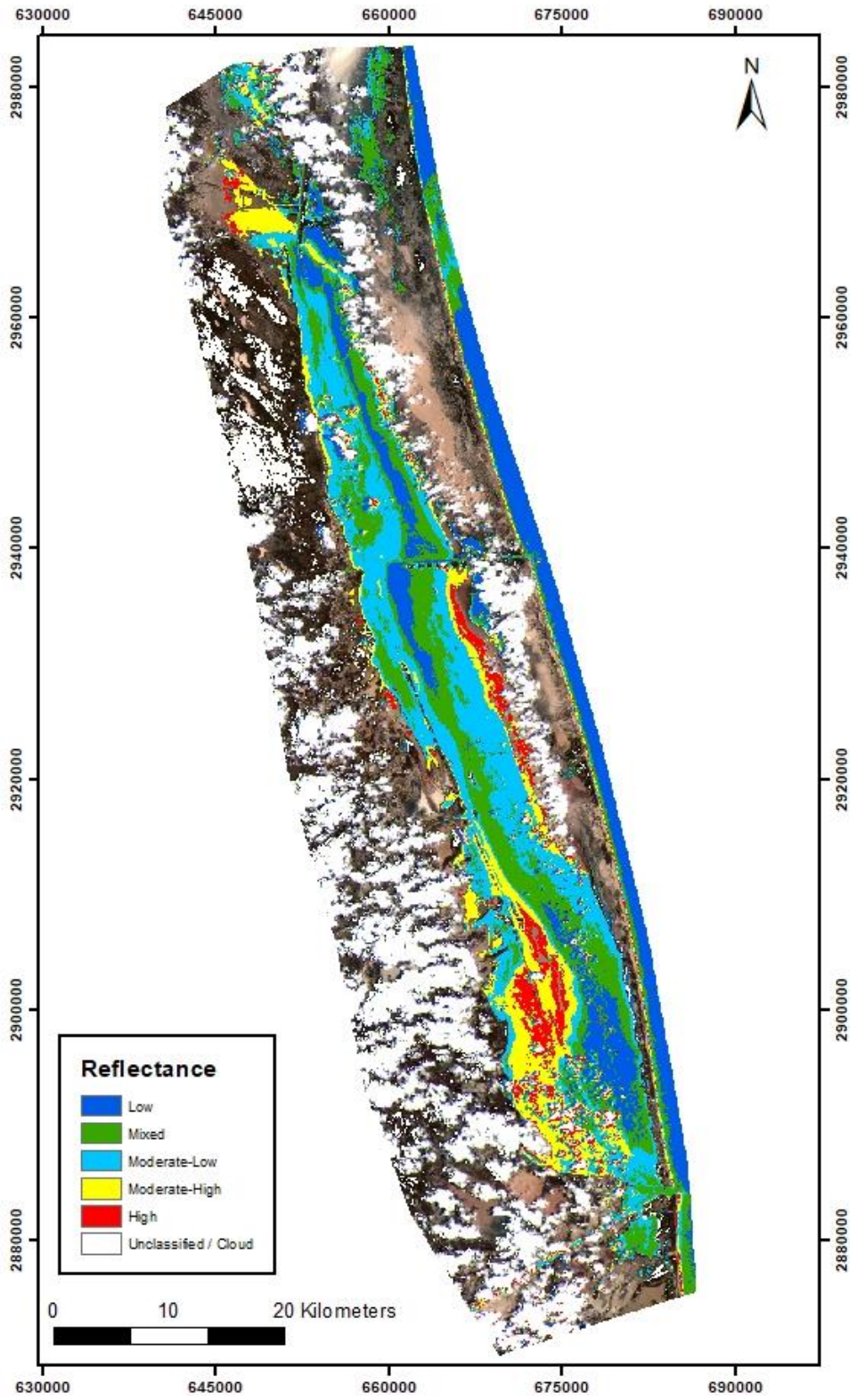

Figure C-4: Surface reflectance as recorded by 27/05/2019 Sentinel-2A L1C Band 5, classified using ENVI v5.5 Spectral Profile Tool. Lagoon water quality has increased, however, there were large areas in the southwest and in the east with high reflectance, corresponding to lower water quality.

Appendix D – Satellite derived bathymetry

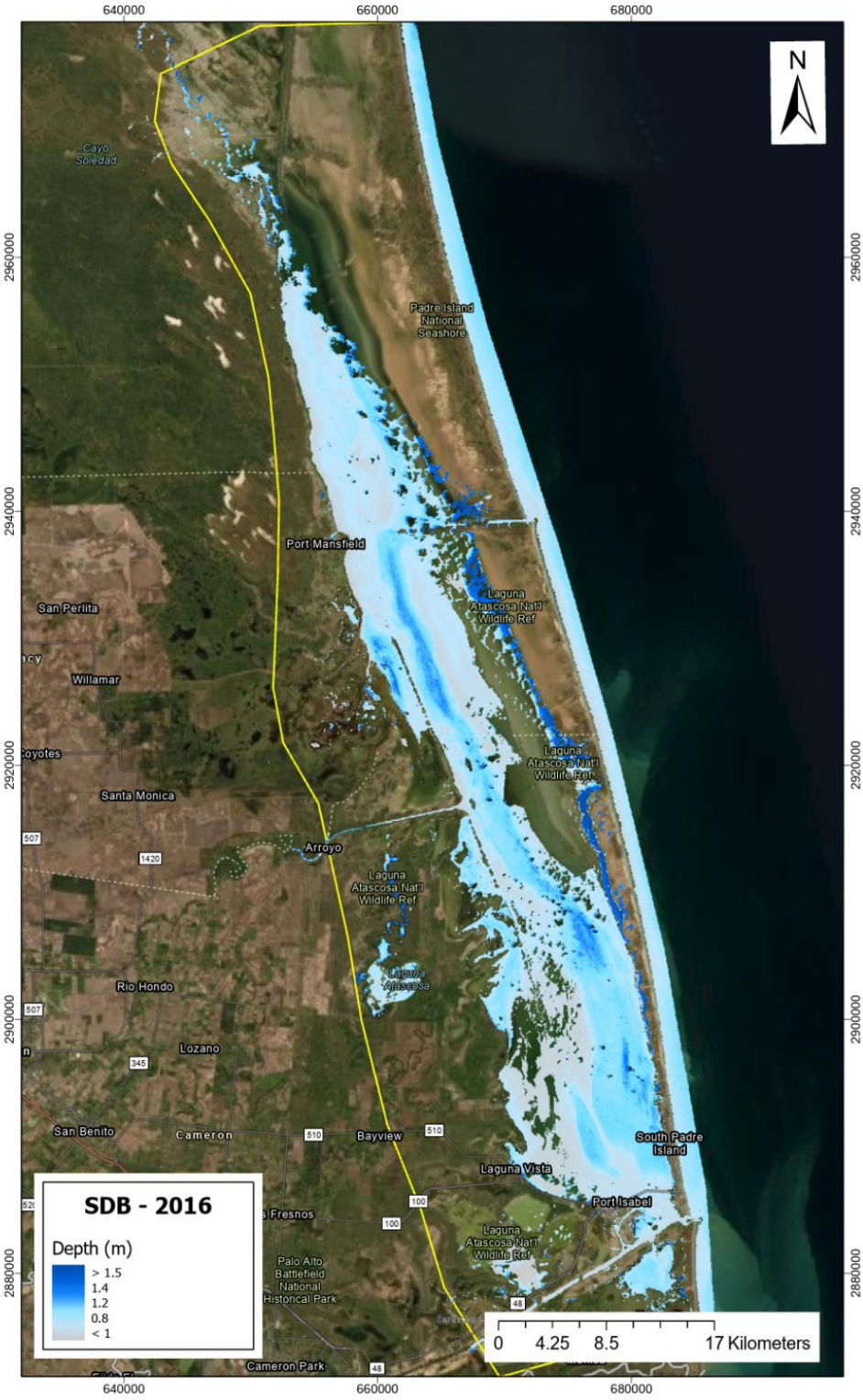

Figure D-1: SDB of Laguna Madre as derived from 05/12/2016 Sentinel-2A L1C imagery. The deepest location measured was 2.34 m.

Figure D-2: SDB of Laguna Madre as derived from 16/06/2017 Sentinel-2A L1C imagery. The deepest area was 1.58 m, and the depth range was calculated at 2.1 m.

Figure D-3: SDB of Laguna Madre as derived from 17/05/2018 Sentinel-2A L1C imagery. Analysis indicated 1.71 m as the deepest, and depth range was 2.24 m.

Figure D-4: SDB of Laguna Madre as derived from 27/05/2019 Sentinel-2A L1C imagery. The depth range and the maximum depth was 2.54 m.